Electrochimica Acta 341 (2020) 136049

Contents lists available at ScienceDirect

Electrochimica Acta

journal homepage: www.elsevier.com/locate/electacta

Electrochemical performance of Bi_2Te_3 heterostructure thin film and Cu_7Te_4 nanocrystals on undoped and In^{3+}-doped WO_3 films for energy storage applications

Supitchaya Buathet [a], Kodchakorn Simalaotao [b, c], Pakpoom Reunchan [b, d], Veeramol Vailikhit [e], Pichanan Teesetsopon [f], Duanghatai Raknual [e], Nareerat Kitisripanya [g], Auttasit Tubtimtae [a, *]

[a] Department of Physics, Faculty of Liberal Arts and Science, Kasetsart University, Kamphaeng Saen Campus, Nakhon Pathom, 73140, Thailand
[b] Department of Physics, Faculty of Science, Kasetsart University, Bangkok, 10900, Thailand
[c] National Metal and Materials Technology Center (MTEC), National Science and Technology Development Agency (NSTDA), Pathum Thani, 12120, Thailand
[d] Thailand Center of Excellence in Physics (ThEP Center), Commission on Higher Education, Bangkok, 10400, Thailand
[e] Department of Chemistry, Faculty of Liberal Arts and Science, Kasetsart University, Kamphaeng Saen Campus, Nakhon Pathom, 73140, Thailand
[f] Department of Physics, Faculty of Science, King Mongkut's Institute of Technology, Ladkrabang, Bangkok, 10520, Thailand
[g] Department of General Science, Faculty of Science and Engineering, Kasetsart University Chalermphrakiat Sakon Nakhon Province Campus, Sakon Nakhon, 47000, Thailand

ARTICLE INFO

Article history:
Received 27 May 2019
Received in revised form
22 December 2019
Accepted 8 March 2020
Available online 11 March 2020

Keywords:
Bi_2Te_3 thin Film
Cu_7Te_4 nanocrystal
Indium doping
Electrochemical performances
Energy storage applications

ABSTRACT

We demonstrated the synthesis of undoped and In^{3+}-doped WO_3 as an electron acceptor for energy storage applications, by utilizing the electrochemical S^{2-} insertion/extraction process at the heterostructure of rhombohedral Bi_2Te_3 thin films and hexagonal Cu_7Te_4 nanocrystals. The cyclic voltammetry of heterostructured electrodes with and without In^{3+} doping both showed Faradic pseudo-capacitance behavior based on the oxidation and reduction processes. The largest exchange current density of 3.43 mA/cm^2 was obtained for the heterojunction-structured-Bi_2Te_3 thin films and Cu_7Te_4 nanocrystals with In^{3+} doping in the WO_3 electrode. This implies more favorable hydrogen evolution reaction kinetics and higher electrocatalytic activity at the anode. The highest specific capacity of 90.2 mA h/g was obtained at a scan rate of 10 mV/s, with the power density reaching 1.7 kW/kg at the highest energy density value of 18.85 Wh/kg for the In^{3+}-doped electrode. The overall results revealed the inherent properties of the new electrode materials, as well as their potential use in energy storage devices or in future electrochemical energy conversion and storage applications involving hydrogen (or oxygen) evolution reactions.

© 2020 Elsevier Ltd. All rights reserved.

1. Introduction

In the past decades, thin film and nanocrystal (NC) semiconductors have attracted much

attention for electrodes in electrochemical devices [1,2]. Fundamental investigations have been conducted on the characteristics and electronic properties of metal chalcogenide semiconductors in the II-VI groups, owing to their notable advantages of low cost, easy large-scale synthesis, and environmental friendliness. However, the synthetic parameters should be further examined to identify suitable candidates for high-tech devices based on the thin films and NCs of these semiconductors. A few researchers have tried to improve bi-layer semiconductor thin films and NCs in developing long-term energy storage technologies that are economical and clean. For example, core-shell structured Fe_3O_4@NiS nanocomposites have been successfully synthesized using a modified sedimentation-oxygenation method, and tested as an anode material for iron-based alkaline rechargeable batteries [3]. A Cu_2S/Ag_2S composite electrode was formed on nickel foam using a successive ionic layer adsorption and reaction (SILAR) technique, and fabricated into a simple and cost-effective high-performance battery-type supercapacitor [4]. Nested CdS@HgS core-shell nanowires, synthesized using a chemical route at room

* Corresponding author.
E-mail address: tubtimtae@gmail.com (A. Tubtimtae).

https://doi.org/10.1016/j.electacta.2020.136049
0013-4686/© 2020 Elsevier Ltd. All rights reserved.

temperature (300 K) without any surfactant or binder, were used as a supercapacitive Faradic electrode and demonstrated a significant supercapacitance of 224.97 F/g at a scan rate of 5 mV/s [5]. A facile method was also reported to fabricate a FeP/CdS composite, which exhibited excellent catalytic activity for H_2 evolution under visible light with lactic acid as a sacrificial reagent [6]. Furthermore, noble-metal-free CdS@MoS_2 core-shell nano-heterostructures exhibited outstanding photocatalytic H_2 evolution performance [7].

These results show that the inherent properties of electrode materials play a crucial role in electrochemical and energy storage applications. Also, understanding the chemical reactions at the interface between the electrode and electrolyte can lead to electrochemical cells with high efficiency and durability. Unfortunately, there has been few studies using binary composites based on a chalcogenide material for electrochemical and energy storage applications.

Based on our knowledge in materials synthesis, bismuth telluride (Bi_2Te_3) is one of the basic materials for high-performance thermoelectric generators with a figure of merit of ~1.14 at room temperature (298 K) [8,9]. In addition, bulk single-crystal Bi_2Te_3 has an extremely low thermal conductivity of ~1.5–2.0 W/m·K along the cleavage plane, and 0.6 W/m·K along the direction of van der Waals interaction [10]. At 300 K, the electron and hole mobilities of Bi_2Te_3 are 1140 and 680 $cm^2/V·s$, respectively [11], with their *n*- and *p*-type electrical conductivities being 1.655×10^3 and $1.4 \times 10^3\ \Omega^{-1}\ cm^{-1}$ [12]. However, the use of this material in electrochemical and energy storage devices has not been thoroughly studied.

Meanwhile, copper telluride ($Cu_{2-x}Te$) is a binary *p*-type semiconductor of type I–VI, with a high thermal conductivity of 4 W/m·K at 300 K [13]. The highest field effect hole mobility reported was ~18 $cm^2/V·s$ [14], in which the crystal structure depended upon the phase value x ($1 \leq x \leq 2$) [15,16], as well as a high carrier concentration of 10^{19}–$10^{22}\ cm^{-3}$ [17]. In addition, the Cu–Te system is highly complex and includes a variety of compounds due to its substantial stoichiometric deviation [16,18].

Dopants are often used to improve or adjust the electrochemical and optical properties of the electron acceptor in devices, by changing the material's Fermi level, characteristics, bonding energy, and electronic structure.

Indium (In^{3+}) as a dopant is relatively cheap and has low toxicity [19]. It displays strong resistance to oxidation at room temperature, and a shorter diffusion path of electrons and ions into the electrode materials. Such properties can improve the nucleation process in nanostructured materials, leading to better utilization of electrochemical active materials and a higher power density [20]. Indium also has the ability to achieve effective charge separation and inhibit carrier recombination in devices [21]. In our previous study, indium was used as a dopant in a TiO_2 photoelectrode with a $Cu_{2-x}Te$ sensitizer for solar cell applications. The results showed that In^{3+} doping improved the power conversion efficiency and decreased the charge transfer resistance (R_{ct}). Moreover, the electron lifetime was improved, owing to the appearance of a trap-state mediator from indium incorporation in the structure and suppression of the charge recombination process [22].

Recent reports have suggested that tungsten oxide (WO_3) can act as a support for noble metals and has electrocatalytic activity for hydrogen evolution [23]. In this study, we applied co-binary Bi_2Te_3 thin film and Cu_7Te_4 NCs on undoped and In^{3+}-doped WO_3 films for use in energy storage applications. The samples were characterized by morphological, optical, and electrochemical measurements. Electronic structure calculations with density functional theory (DFT) was also used to better understand the electron transfer mechanism through the density of states (DOS) and the band gaps of undoped and In^{3+}-doped WO_3 electrodes.

We utilized a facile method that involves three precursor solutions containing Cu^{2+}, Bi^{3+}, and Te^{2-} ions to coat the co-binary Bi_2Te_3 thin film and Cu_7Te_4 NCs on undoped and In^{3+}-doped WO_3 layers. This approach was selected because copper is known to diffuse very rapidly in bismuth telluride at room temperature [24]. Further, the electrode fabrication condition could be adjusted to enhance the electrochemical performance. Further development could overcome the electrically insulating nature in polysulfide electrolyte and electrode materials, in order to achieve high active material utilization especially in stationary photovoltaic and optoelectronic devices. Co-binary metal chalcogenide semiconductors can also be applied in various ways, such as for load leveling, emergency power supply, and uninterruptible power supply. Thus, WO_3 electrodes can be adopted in low-cost, safe, and high-performance electrochemical materials in aqueous Na–S redox electrolytes for energy storage devices in the future.

2. Experimental details

2.1. Preparation of undoped and In^{3+}-doped WO_3 electrodes

A fluorine-doped tin oxide (FTO) glass substrate (sheet resistance ~13 Ω/cm^2, Aldrich) was cleaned using a stepping procedure in a nitric acid:deionized (DI) water (3:7 v/v) solution, acetone, methanol, and DI water for 10 min each in an ultrasonic cleaner. Then, the glass substrate was placed on a hot plate at over 100 °C until it dried.

A WO_3 film was prepared by mixing 0.61 M WO_3 nanopowder (≥99% ACROS, particle size ~35–40 nm), 0.15 M ethyl cellulose (90% Sigma-Aldrich), and 0.37 M terpineol (95% Sigma-Aldrich) in ethanol. Then, the mixed precursors were stirred for 4 h. For performance comparison, 2 wt% $InCl_2$ powder (98% purity, Sigma-Aldrich) was used as source of the indium (In^{3+}) dopant. The undoped and In^{3+}-doped WO_3 solutions were coated on a cleaned FTO glass substrate with an active area of 1 cm^2 using a spin-coating technique. Six layers of the undoped or In^{3+}-doped WO_3 were coated on the glass under conditions of 1500 rpm and 15 s/round. After that, they were sintered at 450 °C for 30 min. The average thickness of the film with or without doping was ~600–700 nm [25]. The characteristics of the undoped and In^{3+}-doped WO_3 electrodes are shown in Fig. S1 of the supplementary data.

2.2. Preparation of copper telluride (Cu_7Te_4) NCs

The undoped and In^{3+}-doped WO_3 films were immersed in a 0.1 M solution of copper (II) nitrate trihydrate ($Cu(NO_3)_2·3H_2O$; 99.5% purity, Loba Chemie) in ethanol for 60 s as a precursor for Cu^{2+}. Then, the films were washed using ethanol and heated on a hot plate until dry. Next, the films were immersed in a 0.1 M Na_2O_3Te methanol:DI water (7:3 v/v) solution for another 60 s as a precursor for Te^{2-}, before being washed again using methanol and drying on a hot plate. These steps are referred to as one SILAR cycle. The WO_3 films were treated for various SILAR cycles ($m = 1$–10) to investigate the optimal SILAR conditions for Cu_7Te_4 NCs.

2.3. Preparation of Bi_2Te_3 thin films

We dissolved 0.1 M bismuth(III) nitrate pentahydrate ($BiN_3O_9•5H_2O$; ≥98%, Sigma-Aldrich) in ethanol, and sodium tellurite (Na_2O_3Te; 99% purity, Sigma-Aldrich) in a mixture of methanol and DI water (7:3 v/v). The two precursor solutions were mixed and stirred for 90 min. Afterward, the Bi–Te solution was dropped onto a WO_3 film and screened using a doctor blading technique to form the Bi_2Te_3 thin film. The Bi_2Te_3 thin film was

heated at 60 °C for a few minutes, and this procedure forms one layer of Bi_2Te_3. Various numbers of layers ($n = 1$–10) were tested to investigate the optimal coating condition of the Bi_2Te_3 thin film.

2.4. Method for electronic structure calculations

Our electronic structure calculations were based on DFT with a screened hybrid functional proposed by Heyd, Scuseria, and Ernzerhoff (HSE06) [26], as implemented in the Vienna Ab initio Simulation Package [27]. Projector-augmented wave potentials with 12, 6, and 3 valence electrons for W ($5p^6 5d^4 6s^2$), O ($2s^2 2p^4$), and In ($5s^2 5p^1$) were used to describe the interactions between the valence electrons and ionic cores. We used a standard mixing parameter of 25% Hartree–Fock exchange, which resulted in a direct Γ–Γ gap of 2.50 eV. This band gap value is much larger compared with that using a semi-local functional, such as the generalized gradient approximation (GGA) at 1.21 eV. Although, the calculated band gap based on the standard HSE functional is still smaller than the experimental value of 3.39 eV, the defect levels and formation energies are expected to be substantially higher compared to the results obtained using the GGA. To simulate the In^{3+} doping in WO_3, we used a 48-atom supercell ($1 \times 1 \times 3$ of the 16-atom primitive cell of WO_3 (space group P21/*a*)). A single special *k*-point (1/4, 1/4, 1/4) was used for integrations over the Brillouin zone of the supercell. The energy cutoff for the plane wave expansion was set to 400 eV, and all atoms were relaxed until the residual forces were less than 0.02 eV/Å. Test calculations using a $2 \times 2 \times 2$ special *k*-point mesh showed that the difference in the formation energy of an indium defect was less than 0.15 eV, and our main results remained valid.

The possibility of forming substitutional or interstitial indium impurities was determined using the formation energy as a function of the tungsten (μ_W) and indium (μ_{In}) chemical potentials for all possible charge states. For example, the formation energy of In_W in charge state q is given by [28].

$$E^f(In_W^q) = E_{tot}(In_W^q) - E_{tot}(WO_3) - \mu_{In} + \mu_W + q(E_F + E_V), \quad (1)$$

where $E_{tot}(In_W^q)$is the total energy of the supercell containing one indium substituted for an In (In_W), and $E_{tot}(WO_3)$is the total energy of the same perfect supercell. The indium atom is taken from a reservoir with energy $\mu_{In} = \tilde{\mu}_{In} + E_{tot}[In_{metal}]$, and the W atom is placed in a reservoir with energy$\mu_W = \tilde{\mu}_W + E_{tot}[W_{metal}]$. The chemical potentials ($\tilde{\mu}$) can be varied to represent the experimental conditions during growth or annealing, which can range from O-rich (W-poor) to O-poor (W-rich). In equilibrium growth of the WO_3 crystal, the chemical potentials $\tilde{\mu}_W$ and $\tilde{\mu}_O$must satisfy the stability condition $\tilde{\mu}_W + 3\tilde{\mu}_O = \Delta H_f(WO_3)$, where $\Delta H_f(WO_3)$ is the enthalpy of WO_3 formation. Our calculated $\Delta H_f(WO_3)$ is −8.55 eV, which is in good agreement with the experimental value of −8.72 eV (monoclinic phase) [29]. The indium chemical potential is limited by the formation of In_2O_3 $\tilde{\mu}_{In} = (\Delta H_f(In_2O_3) - 3\tilde{\mu}_O)/2$. For the intermediate growth condition, $\tilde{\mu}_O$was calculated via the expression described in Ref. [30]. The sintering temperature of 450 °C at the oxygen partial pressure under ambient conditions corresponded to $\tilde{\mu}_O = -0.68$ eV. The formation energy also depends on the Fermi level E_F, which represents the energy of the electron reservoir in WO_3 and is conventionally referenced to the valence band maximum (VBM) of the host material (E_V).

2.5. Investigation of vibration modes, chemical compositions, and morphological characteristics

The vibration modes of elements were investigated using a Raman spectroscope (HORIBA Jobin Yvon S.A.S. Model T64000 triple monochromator) with 532 nm excitation from a solid-state laser at 150 mW. X-ray photoelectron spectroscopy (XPS) analysis was performed to identify the chemical states in the as-prepared electrodes using an AXIS Ultra DLD (Kratos Analytical Ltd.) with a soft X-ray beam produced from a monochromated Al Kα anode source. The energy of incident photons was 1486.6 eV, with calibration based on the spectrometer's work function and the Fermi energy level (E_f). The obtained XPS spectra were calibrated against the C1s photoelectron peak at 285 eV from contamination, in order to compensate for the surface charge energy. The synthesized thin films were characterized using a field-emission scanning electron microscope (JEOL, JSM-6301 F), with an energy dispersive spectroscope (INCA, PentaPET × 3) to examine the stoichiometry of elements in the structures. An X-ray diffractometer with Cu-K_α at 1.5406 Å (D8 Advance, Bruker AXS) was used to determine the X-ray diffraction (XRD) patterns of the structure in the range $10^\circ \le 2\theta \le 80^\circ$ with a resolution of 0.01°.

2.6. Electrochemical measurements

Our cyclic voltammetry (CV), chronoamperometry (CA), chronocoulometry (CC), and linear sweep voltammetry (LSV) analyses all used the electrochemical insertion/deinsertion of sulfur ion to indicate the charge transfer ability in undoped and In^{3+}-doped WO_3 films to an external circuit. During the CV process, an electrochemical analyzer (PGSTAT101, Metrohm Autolab) with scan rates of 10, 30, 50, 70, and 100 mV/s was used in a conventional three-electrode system. A deposited heterostructured film on an FTO glass with an active area of 1 cm^2 was used as a working electrode, CuS as a counter electrode, and integrated Ag/AgCl in a saturated KCl solution as a reference electrode in a polysulfide electrolyte solution containing 0.25 M $Na_2S \cdot 9H_2O$, 1 M Sulfur, 0.2 M KCl, and 0.1 M KI dispersed in a methanol-water (7:3 v/v) mixture. The CuS counter electrode was prepared and developed based on a previous study [31]. The mass of the films under each condition was measured using a four decimal place balance (OHAUS Corporation, USA).

3. Results and discussion

3.1. Electronic structure calculations

Here, we focus on the effects of In^{3+} doping on the electronic properties of WO_3. Our calculated formation energies for indium substituted for tungsten (In_W) and indium interstitial (In_i) for the O-poor, experimental, and O-rich conditions are shown in Fig. 1(a–c), respectively. We found that In_i exclusively occurs in the 3+ charge state, acting as a triple donor for all Fermi-level values in the band gap. This electron donor behavior of In_i is expected, because at the interstitial site, the In^{3+} atom donates its three valence electrons to the six surrounding O atoms (Fig. 2(a)). Thus, the oxidation state of In_i can be expected to be 3+. However, its actual oxidation state requires further analysis, which is beyond the scope of the present study. On the other hand, In_W (Fig. 2(b)) is expected to be an electron acceptor, since In^{3+} ions are likely to have a 3+ oxidation state when surrounded by six O atoms and the oxidation state of W ions in WO_3 is likely to be 6+. Actually, we found that In_W acts as a triple acceptor and is stable in the neutral, 1-, 2-, and 3- charge states.

Our calculated formation energies indicated that In_i is a prevalent defect for most Fermi-level values in the gap, ranging from the VBM to ~0.35 eV below the conduction band minimum (CBM) for the experimental growth condition (sintering at 400 °C in air). However, In_W becomes prevalent for the Fermi-level values near

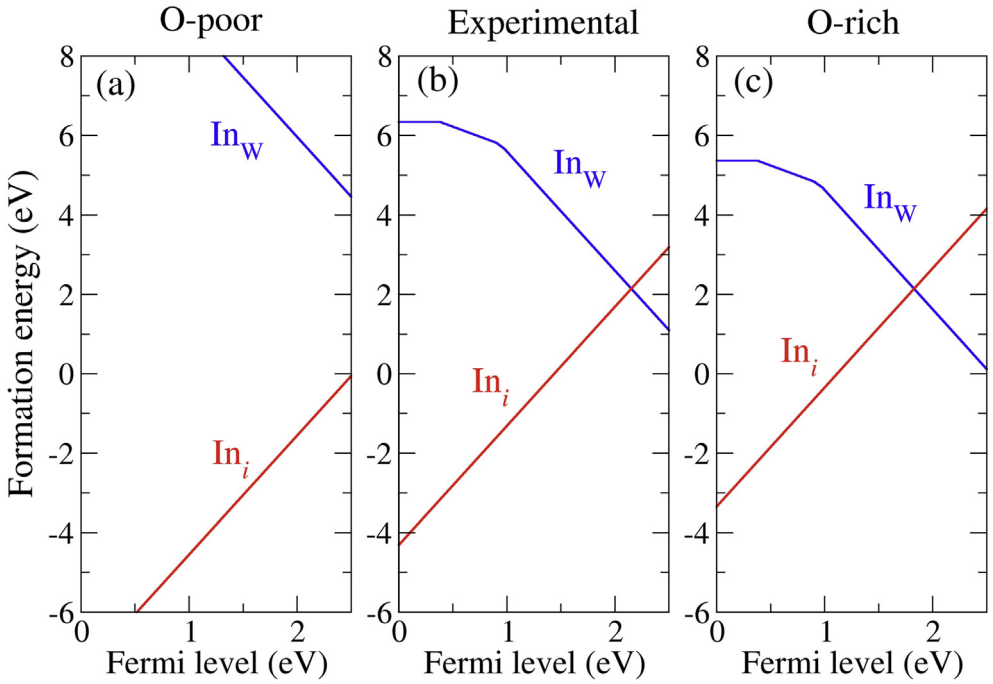

Fig. 1. Formation energies of In-related defects as a function of Fermi level ranging from 0 to the calculated band gap of 2.49 eV under (a) O-poor, (b) experimental, and (c) O-rich growth conditions. The slope of the line indicates the charge states of the defects.

the CBM. Assuming that the dominant defects in In^{3+}-doped WO_3 are governed by In^{3+} impurities, the pinned Fermi level can thus be determined by balancing the concentrations between charged In_W, In_i, and free carriers. As a result, the Fermi level virtually corresponds to the intersection of the two lines for In_W (In_W^{3-}) and In_i (In_i^{3+}) at ~0.35 eV below the CBM. Thus, In^{3+}-doped WO_3 is likely to exhibit *n*-type conductivity. As the oxygen partial pressure (oxygen chemical potential) is lowered toward the O-poor condition, the formation energy of In_i decreases, resulting in the prevalence of In_i for the entire range of Fermi-level values in the gap. For the O-poor condition, the Fermi level of In^{3+}-doped WO_3 is located at the CBM, and thus, the material becomes *n*-type.

Because the formation energies of In_W^{3-} and In_i^{3+} (and also their concentrations) were almost identical for the experimental growth conditions, the electronic structures of these two impurities in their stable charge states were examined via the DOS shown in Fig. 3. Fig. 3(a) shows the DOS of the pristine WO_3 supercell. From Fig. 3(b and c), we found that neither In_i nor In_W induce defect levels in the band gap of the pristine WO_3 supercell. For In_i (Fig. 3(b)), the In *s* state is resonant in the conduction band, while for In_W (Fig. 3(c)) the In *s* state is split into low- and high-energy states that are deep in the valence band and high in the conduction band, respectively.

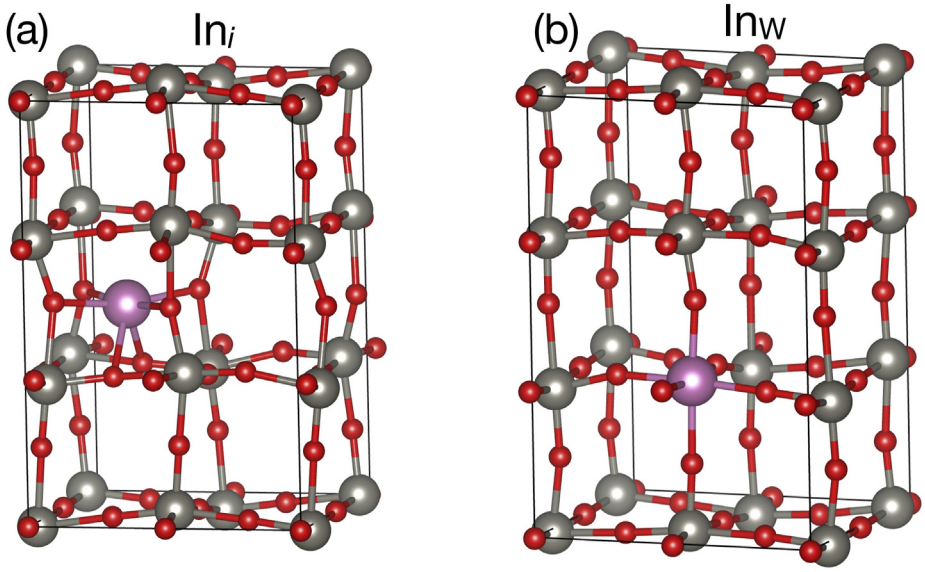

Fig. 2. Atomic structure of WO_3 supercell containing (a) indium interstitial (In_i) and (b) indium substituted for W (In_W). The gray, red, and violet balls represent W, O, and In atoms, respectively. (For interpretation of the references to color in this figure legend, the reader is referred to the Web version of this article.)

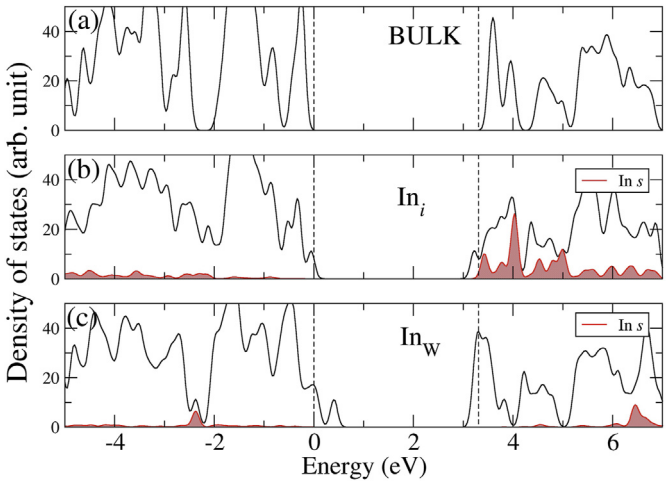

Fig. 3. Density of states (DOS) of (a) the defect-free WO_3 supercell, (b) the same supercell containing In_i in 3+ charge state, and (c) In_W in 3− charge state. The unfilled curve in each panel is the total DOS and the filled curve is the DOS projected on the In *s* state (scaled up by a factor of 20 for clarity). The dashed lines indicate the calculated VBM (left) and CBM (right) of the pristine WO_3 supercell. The DOS of supercell with the In^{3+} impurity is aligned with that of the defect-free supercell using the average electrostatic potential at the core of W and O atoms located far away from the In^{3+} impurity.

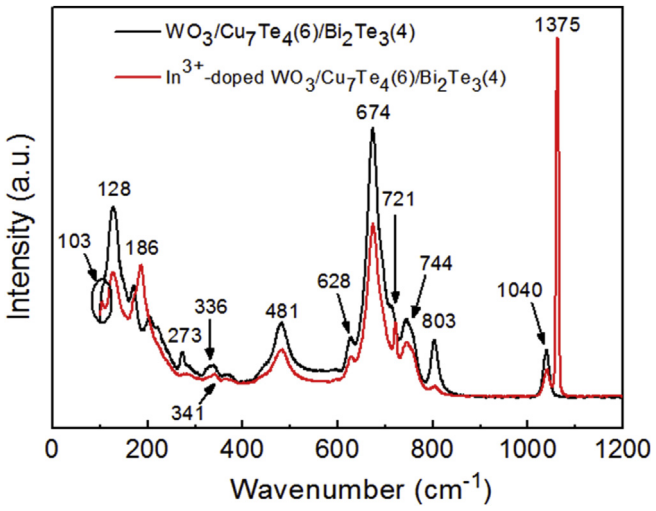

Fig. 4. Raman spectra of $Cu_7Te_4(6)/Bi_2Te_3(4)$-coated undoped and In^{3+}-doped WO_3 electrodes.

However, these In^{3+} impurities introduce a downward shift of the conduction band edge and an upward shift of the valence band edge. These shifts resulted in an absorption edge of ~0.8 eV, which is narrower than that of the undoped WO_3 (~2.5 eV).

3.2. Raman spectroscopy measurement

Fig. 4 shows the Raman optical phonon spectra for $WO_3/Cu_7Te_4(6)/Bi_2Te_3(4)$ and In^{3+}-doped $WO_3/Cu_7Te_4(6)/Bi_2Te_3(4)$ at room temperature (298 K). The peaks for WO_3 were observed at 273 and 803 cm^{-1} and correspond to two characteristic bands. The first band between 200 and 500 cm^{-1} was assigned to the O—W—O bending vibration modes, and the second band between 600 and 1000 cm^{-1} was attributed to the W—O stretching vibration mode. However, the peak of 186 cm^{-1} may have been due to the presence of the orthorhombic $WO_3 \cdot (1/3)H_2O$ structure [32]. The peaks at 103 and 128 cm^{-1} could be respectively identified as the Raman active modes of E^2_{1g} and A^2_{1g} for Bi_2Te_3. In the E_g modes, the atoms vibrate in a two-dimensional plane and perpendicular to the [111] direction, while in A_{1g} modes, the atoms vibrate in a one-dimensional plane along the [111] direction in the rhombohedral cell. The presence of the van der Waals gap between the quintuple layers resulted in a preferential cleavage plane between the outmost adjacent $Te^{(1)}$ layers with the sequence of $Te^{(1)}$—Bi—$Te^{(2)}$—Bi—$Te^{(1)}$, where the superscripts (1) and (2) refer to the two different chemical states of the Te anions. Thus, the formation of these anisotropic crystallographic features make it possible to fabricate nanostructured Bi_2Te_3 [33]. Moreover, weak bands at 336 and 341 cm^{-1} of Cu—O were assigned to the Cu—O—NO_2 (nitrate) and Cu—O—ClO_3 (perchlorate salts) stretching vibration modes, respectively [34]. The 481 cm^{-1} band was assigned to vibrationally isolated Si—O—Si, Si—O—B modes from the borosilicate slide glass substrate [35]. The 628 and 674 cm^{-1} peaks corresponded to the stretching vibration of TeO_4 trigonal bipyramids (tbp) [36]. The peak observed at 674 cm^{-1} may also be attributed to stretching modes arising from W—OH_2, which is consistent with the presence of $WO_3 \cdot H_2O$ phases [37]. The low band peak at 721 cm^{-1} indicated the bending of three equivalent Te—O bonds: one Te═O and two Te—O^- bonds from the TeO_3^{2-} group in Na_2TeO_3 [38]. In addition, the relative intensity of the peak at 744 cm^{-1} slightly increased, indicating the transformation of the TeO_4 tbp into a TeO_3 trigonal pyramid (tp) and TeO_{3+1} polyhedra [39]. The band ranging from 400 to 450 cm^{-1}, which is related to the In—O stretching modes for the undoped and In^{3+}-doped WO_3 electrodes, was not observed in our results. A possible explanation is the low concentration of In^{3+} atoms incorporated in WO_3, which means fewer water molecules attached to the In atoms and consequently a very low peak intensity in the Raman spectrum [40]. Considering actual ion symmetry, the Raman and infrared active modes (at 1040 and 1375 cm^{-1}, respectively), were related to the ONO_2^- stretching vibration modes [34].

3.3. XPS analysis

The survey spectra of XPS profiles for the undoped WO_3, In^{3+}-doped WO_3, and In^{3+}-

doped $WO_3/Cu_7Te_4(6)/Bi_2Te_3(4)$ films are shown in Fig. 5(a—c), respectively. In all prepared electrodes, the expected chemical elements displayed the corresponding spectra. Based on Fig. 5(a and b), the W 4f core level split into the doublet W $4f_{5/2}$ (37.7 eV) and W $4f_{7/2}$ (35.6 eV) in high-resolution XPS spectra, as shown in Fig. 5(d), corresponding to W in two oxidation states. Then, fitting results of the O 1s core level (Fig. 5(e)) revealed four component peaks. The main peaks at 530.4 eV was correlated with oxygen with strong W═O bond in the metal oxide (WO_3) [41]. The peak at 531.4 eV corresponded to the oxygen in OH and C═O groups [42]. Meanwhile, the peak at ~532.5—533.2 eV was assigned to water molecules adsorbed on the sample surface, confirming that the $WO_3 \cdot H_2O$ phase was formed on the sample surface [43]. The oxidation states of In in WO_3 were assigned based on In $3d_{5/2}$ at 444.3 eV and In $3d_{3/2}$ at 451.9 eV (Fig. 5(f)), which are attributed to indium oxide hydroxide (InOOH) and indium hydroxide ($In(OH)_3$), respectively; and these compounds can be transformed to indium oxide (In_2O_3) [44].

Based on the XPS survey spectrum for $Cu_7Te_4(6)$ and $Bi_2Te_3(4)$ coated on the In^{3+}-doped WO_3 electrode (Fig. 5(c)), the Cu2p region can be split into Cu $2p_{3/2}$ and Cu $2p_{1/2}$ at 934.7 and 954.4 eV, respectively, which characterize CuO (Cu^{2+}) formation (Fig. 5(g)). Two smaller peaks (932.8 and 952.7 eV) were identified by deconvoluting the major peaks, corresponding to Cu_2O (Cu^0/Cu^{1+})

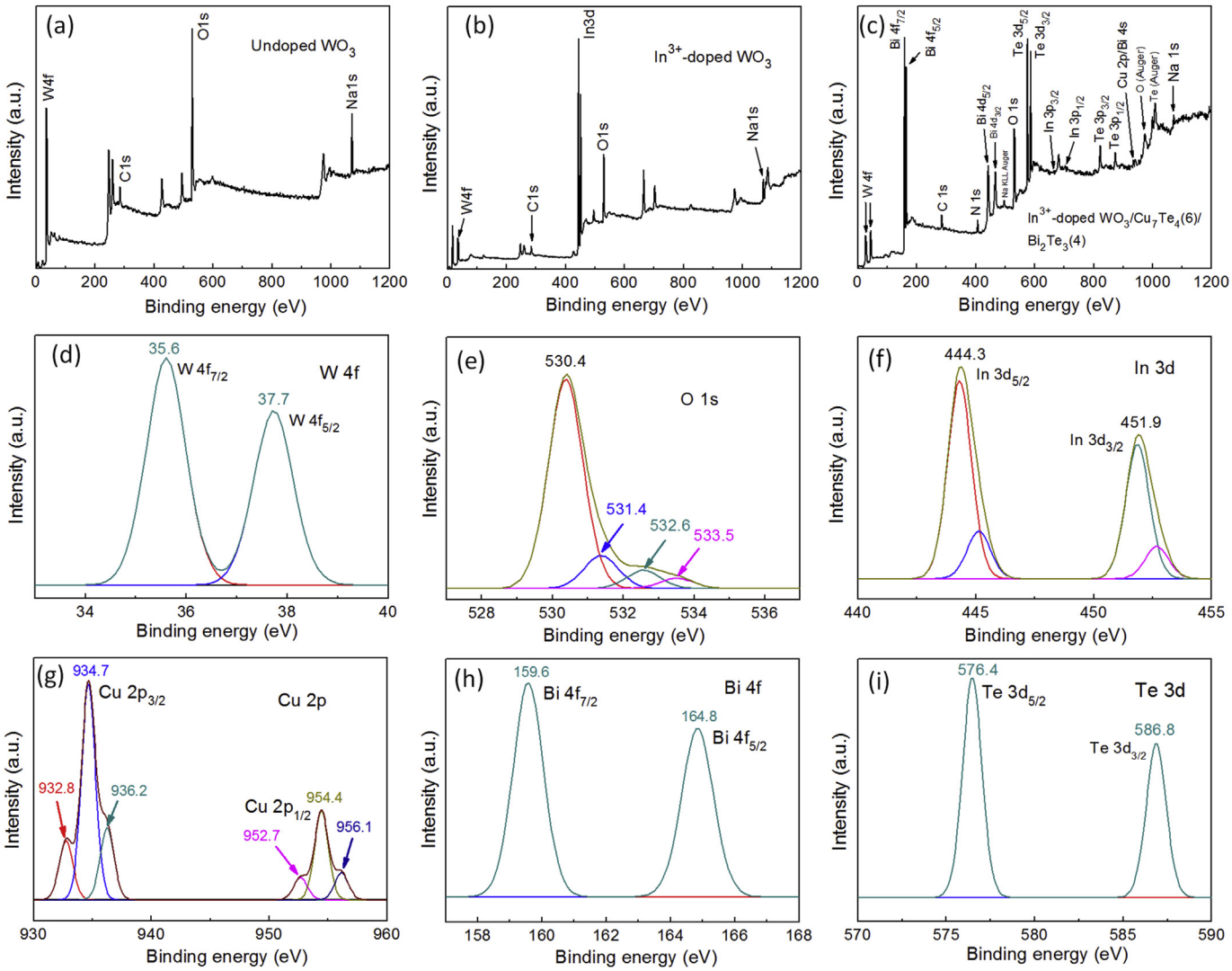

Fig. 5. XPS survey spectrum of (a) undoped WO_3, (b) In^{3+}-doped WO_3, and (c) In^{3+}-doped $WO_3/Cu_7Te_4(6)/Bi_2Te_3(4)$ electrodes. High-resolution XPS spectra of (d) W 4f, (e) O 1s, (f) In 3d, (g) Cu 2p, (h) Bi 4f, and (i) Te 3d.

[45]. However, there were additional peaks at 936.2 eV (Cu $2p_{3/2}$) and 956.1 eV (Cu $2p_{1/2}$), which are consistent with the copper hydroxide ($Cu(OH)_2$) species and demonstrate the existence of Cu^{2+} on the surface of the electrode [46,47]. Furthermore, the two peaks of Bi 4f (Fig. 5(h)), at the binding energies of 159.6 eV for Bi $4f_{7/2}$ and 165.1 eV for Bi $4f_{5/2}$, correspond to Bi^{3+} in the short Bi–O bonds [48] and indicate the existence of bismuth suboxides, Bi(+3−x), due to a deficiency in oxygen and an enhanced concentration of oxygen vacancies near the bismuth cations [49]. Finally, in Fig. 5(i), the Te 3d region is separated into Te $3d_{5/2}$ at 576.4 eV and Te $3d_{3/2}$ at 586.8 eV. These peaks represent the binding energy for Te in TeO_2, and suggest a change in the oxidation state from Te to Te^{2-} due to the difference in its oxidation state of this element [50].

From the results of Raman spectroscopy and XPS analysis, the incorporation of oxygen atom with the chemical elements during preparation leads to a change in the oxidation state and presents a new bonding of compounds as defect-like oxygen vacancies. These effects have been known to influence the electronic structures, physical properties, and the formation of nucleation centers for phase transformation, causing a decrease in the intercalation between cations and anions during the ion intercalation and extraction processes [51].

3.4. Morphological characteristics

The field-emission scanning electron microscopy (FE-SEM) images displayed overall robust evidence for structural characteristics that could affect the electrochemical performance. Fig. 6(a) shows that after In^{3+} doping in bare WO_3, the surface area increased due to the aggregated NCs (Fig. 6(b)). Results after coating the single Cu_7Te_4 NCs, single Bi_2Te_3, and double-layered $Cu_7Te_4(6)/Bi_2Te_3(4)$ on the undoped and In^{3+}-doped WO_3 electrodes are shown in Fig. 6(c–f), respectively. The morphological characteristics did not change substantially, as the particles were all well dispersed with a particle size of ~100–200 nm. However, the double-layered $Cu_7Te_4(6)/Bi_2Te_3(4)$ had a more aggregated, denser, and rougher surface that was mesoporous. This would facilitate electrolyte penetration and ion transportation through the surface of the electrodes. Fig. 7(a and b) display the energy dispersive X-ray spectroscopy (EDS) data for the undoped and In^{3+}-doped WO_3 $Cu_7Te_4(6)/Bi_2Te_3(4)$ electrodes, respectively. The approximate atomic ratios were Cu:Te = 10:7 (that is, 1.43:1) and Bi:Te = 3:5 (that is, 1:1.67) both before and after In^{3+} doping, implying that the non-stoichiometric formulas in the coating were close to Cu_7Te_4 and Bi_2Te_3, respectively. To confirm the crystalline phase of both

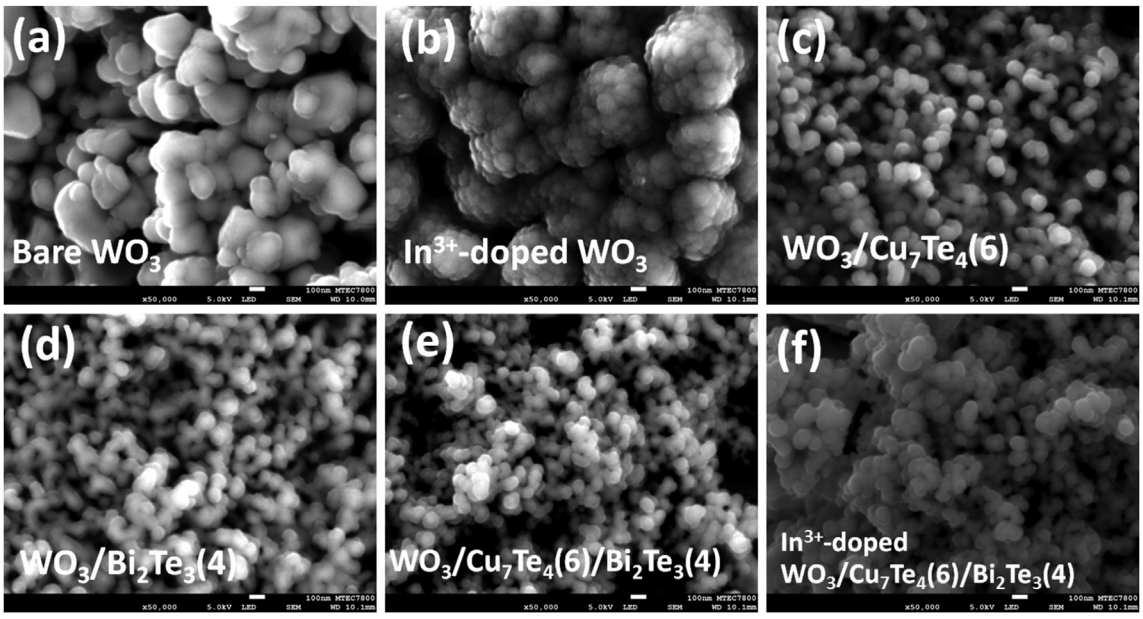

Fig. 6. Scanning electron micrographs of (a) bare WO_3, (b) In^{3+}-doped WO_3, (c) $WO_3/Cu_7Te_4(6)$, (d) $WO_3/Bi_2Te_3(4)$, (e) $WO_3/Cu_7Te_4(6)/Bi_2Te_3(4)$, and (f) In^{3+}-doped $WO_3/Cu_7Te_4(6)/Bi_2Te_3(4)$. Scale bar: 100 nm.

materials, the XRD patterns of the single- and double layer coated on WO_3 surfaces were compared with those of bare WO_3 and In^{3+}-doped WO_3 films (Fig. 7(c)). The peaks of Cu_7Te_4 and Bi_2Te_3 could also be seen for the double-layered structure before and after In^{3+} doping in WO_3. The Cu_7Te_4 NCs had a hexagonal crystal structure with lattice constants of $a = b = 8.280$ Å and $c = 7.220$ Å (JCPDS No. 89–2402). The Cu_7Te_4 peaks at ~40, 50, 77, and 78° corresponded to the (031), (213), (035), and (234) planes, respectively. The Bi_2Te_3 thin film contained a rhombohedral crystal structure with lattice constants of $a = b = 4.395$ Å and $c = 30.440$ Å (JCPDS No. 82–0358).

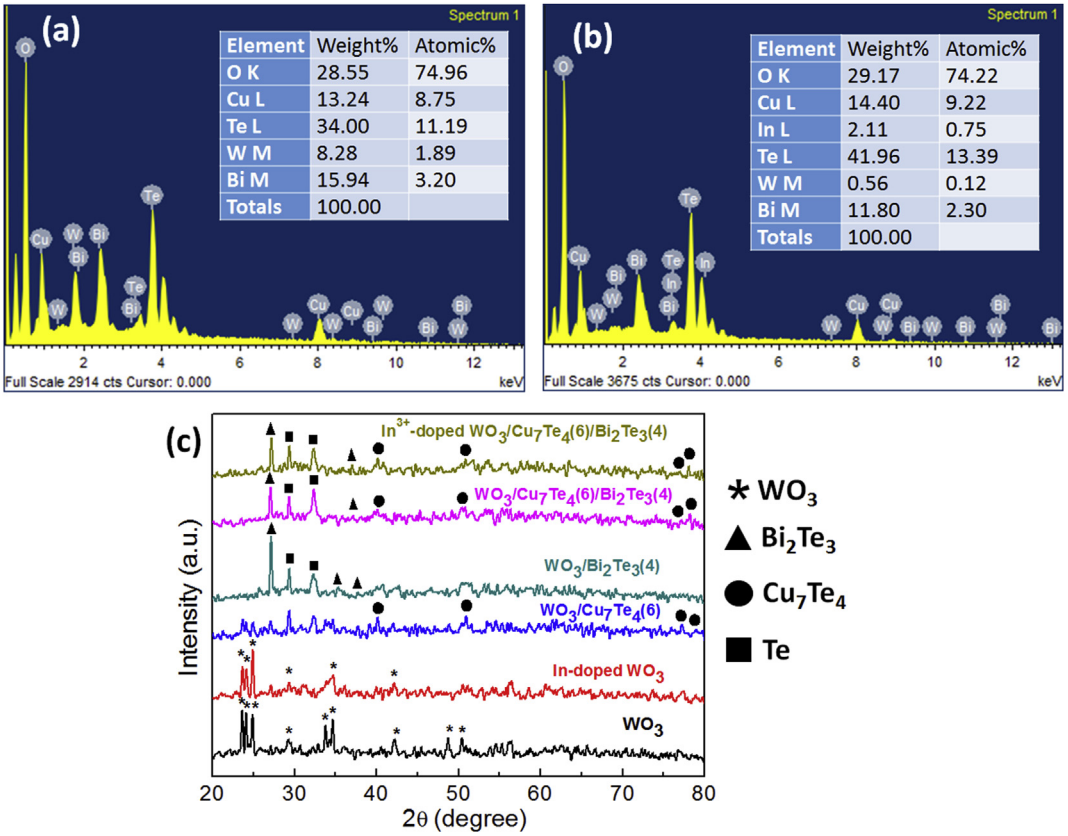

Fig. 7. Energy dispersive X-ray spectra of (a) $WO_3/Cu_7Te_4(6)/Bi_2Te_3(4)$ and (b) In^{3+}-doped $WO_3/Cu_7Te_4(6)/Bi_2Te_3(4)$. (c) X-ray diffraction patterns for various conditions.

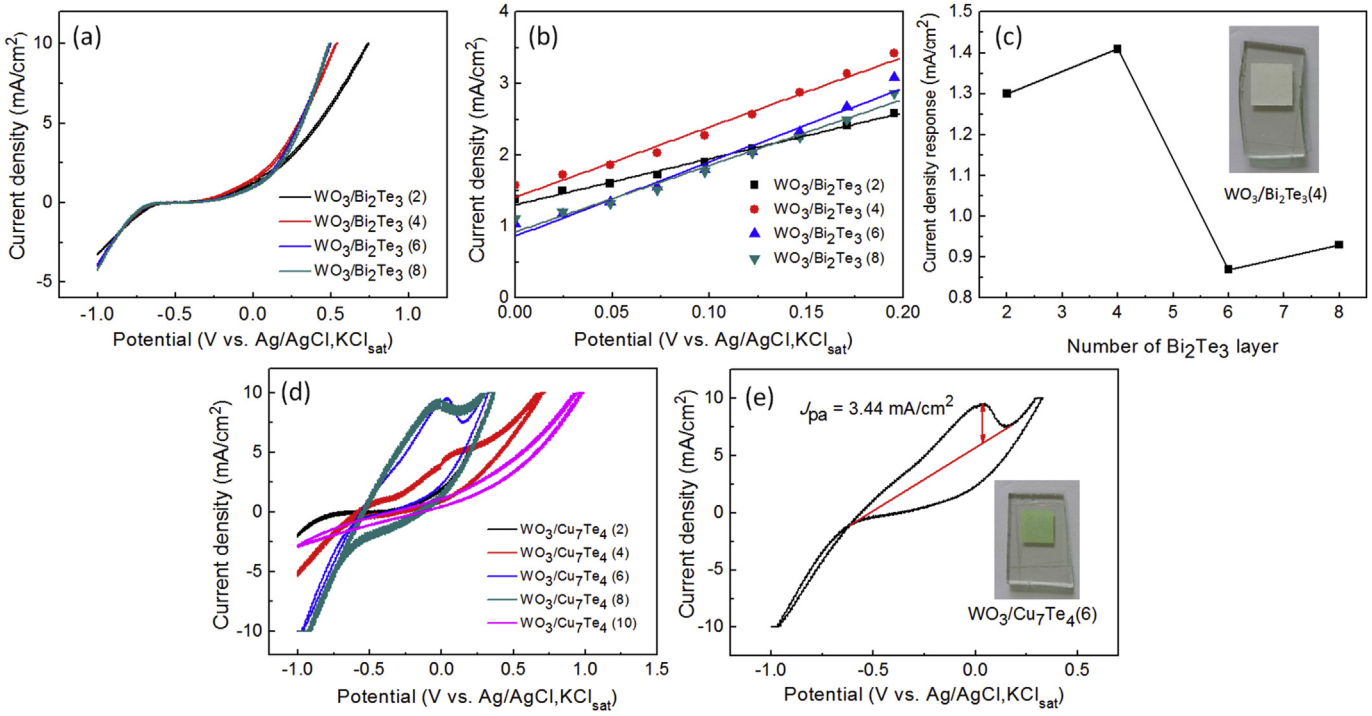

Fig. 8. (a) Cyclic voltammetry measurements of Bi_2Te_3, (b) linear fitting of CV curve under applied potential range from 0 V to 0.2 V, (c) current density response for various Bi_2Te_3 layers, (d) cyclic voltammetry measurements of Cu_7Te_4 at various cycles, and (e) maximum anodic peak current for the optimum SILAR cycle of Cu_7Te_4 coated on the WO_3 electrode.

The most intense peak was that for the (015) plane at ~27°, and the (10$\underline{1}$0) peak at ~37° was observed with a lower intensity. However, the peaks at ~29 and 32° indicated the Te element (JCPDS No. 89–6043), possibly due to imperfect growth during the coating preparation of the Cu_7Te_4 NCs and Bi_2Te_3 thin films. In sum, the material phases identified from the XRD patterns conformed to the non-stoichiometric formula from the EDS analysis.

3.5. Cyclic voltammetry

Fig. 8 shows the electrochemical bleaching oxidation (anodic peak) and coloration

reduction (cathodic peak) in the CV curves of different electrode samples. In the cathodic scan, the curve was at negative potential, and the current steadily decreased to reach a limiting negative value depending on the potential range that corresponds to the coloration of the electrode. In contrast, in the anodic scan, the current moved from a negative potential range to a positive one, and reached the maximum current value before decreasing to near zero, which is indicative of bleaching of the electrode [52]. Fig. 8(a) depicts the dependence of the amperometric response in the cyclic voltammograms of WO_3 electrodes with 2–8 coated Bi_2Te_3 layers in the potential range between −1.0 and + 1.0 V vs. Ag/AgCl. There were well-defined reversible redox peaks corresponding to the electron-hole reversible reaction. The current density response (J_{pa}) for different layers was estimated via the *y*-axis intercept of the fit in the linear region of the CV curve under an applied potential range from 0 to 0.2 V, as shown in Fig. 8(b). The optimum result was found for four layers ($n = 4$), which showed the highest J_{pa} of 1.41 mA/cm^2 (Fig. 8(c)). However, in Fig. 8(d), there were clearly oxidation peaks for the Cu_7Te_4 NCs-coated WO_3 electrode with different SILAR cycles. The J_{pa} increased gradually with increasing SILAR cycles, and at $m = 6$, the WO_3 electrode coated with Cu_7Te_4 NCs had a maximum oxidation peak or anodic peak ($J_{pa} = 3.44$ mA/cm^2) (Fig. 8(e)). When $m > 6$, the maximum oxidation peak tended to decrease gradually, owing to a lower electrochemical activity and smaller capacitance. In the cathodic potential range from −0.5 to −1.0 V, a sharp curve with a high cathodic current density appeared and indicated that the cathodic current density decreased from −2.5 to −10 mA/cm^2, which was affected by the faster kinetics of reduction resulting in inter-valence charge transfer reactions [53]. These results indicated that the sample with $n = 4$ and $m = 6$ exhibited better electrocatalytic activity and electrical conductivity, suggesting that the corresponding electrochemical oxidation should be reacted under a diffusion-controlled process at the interlayer surface of the modified electrode [54].

Excess Bi_2Te_3 layers and SILAR cycles of Cu_7Te_4 NCs prevented the penetration of the electroactive substance toward the electrode surface, resulting in a slower electron transfer rate [32]. Thus, the CV performance was further evaluated for $n = 4$ and $m = 6$, as shown in Fig. 9(a). However, the WO_3 electrode with Bi_2Te_3(4) thin films and subsequently coated by Cu_7Te_4(6) NCs yielded the lowest oxidation peak (J_{pa} = 1.37 mA/cm^2, Fig. 9(b)), while that with Cu_7Te_4(6) NCs underneath Bi_2Te_3(4) thin films produced the highest J_{pa} (3.94 mA/cm^2, Fig. 9(c)) with an observable high negative cathodic current density. The J_{pa} of this co-binary material was even higher than that of the film coated with Cu_7Te_4(6). The In^{3+} doped WO_3 electrode with Cu_7Te_4(6) NCs coated by Bi_2Te_3(4) thin films also showed a distinctly broader and lower anodic coloration peak. The slightly lower J_{pa} of 3.51 mA/cm^2 caused a lower negative cathodic bleaching peak (see Fig. 9(d)), which is attributed to the slower discharge process due to the slower oxidation kinetics and the reduced charge transfer into the film, and some electrons were consumed by oxidizers. This process indicated that the In^{3+} cation diffused inside the WO_3 lattice and was involved in the insertion-removal exchange process of electrons injected into the conduction band of WO_3, which is a reversible process [55]:

$$WO_3 + 3xe^- + xIn^{3+} \leftrightarrow In_xWO_3 \text{ (colored)}. \quad (2)$$

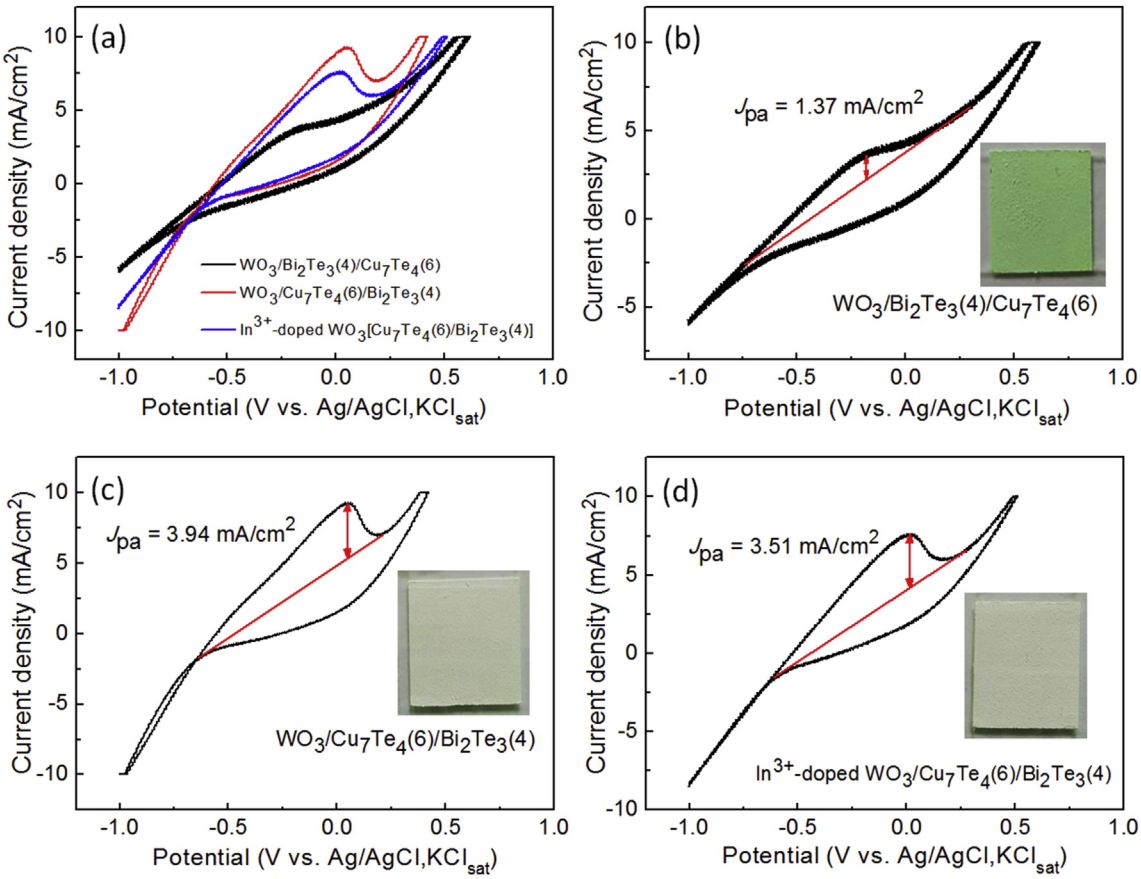

Fig. 9. (a) Cyclic voltammetry measurements of double-layered conditions. Maximum anodic peak current for various conditions of co-binary material coated on the WO_3 electrode: (b) $WO_3/Bi_2Te_3(4)/Cu_7Te_4(6)$, (c) $WO_3/Cu_7Te_4(6)/Bi_2Te_3(4)$, and (d) In^{3+}-doped $WO_3/Cu_7Te_4(6)/Bi_2Te_3(4)$.

Furthermore, the shift in the anodic coloration peak toward higher potentials led to a larger potential separation between the oxidation and reduction processes [56].

The electrode performance basically described by the Tafel plot, which is derived from the steady-state polarization curves. The plot can be fitted by linear regression using the Tafel equation, $\eta = a + b\log|J|$, where η is the applied potential, a is the intercept, b is the Tafel slope, and J is the current density [57]. A smaller Tafel slope provides an advantageous electronic effect. Meanwhile, an increase in the exchange current density (J_0) or the intercept with the potential axis comes from an enhancement in the surface area, which is desirable and measures the inherent electrocatalytic behavior [58,59]. Fig. 10 illustrates the linear regions of the Tafel plots. The Tafel slope is smaller for the $WO_3/Cu_7Te_4(6)/Bi_2Te_3(4)$ electrode (59 mV/dec) compared with those of $WO_3/Bi_2Te_3(4)/Cu_7Te_4(6)$ and In^{3+}-doped $WO_3/Cu_7Te_4(6)/Bi_2Te_3(4)$, which are similar (78 and 75 mV/dec, respectively). Meanwhile, the corresponding J_0 values were estimated to be 2.97, 2.52, and 3.43 mA/cm^2. The largest J_0 of the heterojunction structure with the In^{3+}-doped WO_3 electrode may imply more favorable kinetics for hydrogen evolution reaction (HER) and a higher electrocatalytic activity at the anode [59].

To compare the electrochemical performance of the undoped and In^{3+}-doped $WO_3/Cu_7Te_4/Bi_2Te_3$, CV tests were systematically conducted at scan rates of 10, 30, 50, 70, and 100 mV/s, as depicted in Fig. 11(a and b), respectively. Scanning was also performed with a linear potential sweep between −1.0 and + 1.0 V vs. Ag/AgCl. The CV curves of the undoped and In^{3+}-doped electrodes showed Faradic pseudocapacitance behavior with reversibility in the two pairs of redox response at various scan rates, which may have resulted from the intercalation and deintercalation effects of disulfide ions from the polysulfide electrolyte into the electrode [60,61]. Furthermore, CV curves for the undoped and In^{3+}-doped electrodes had almost identical redox peaks, suggesting similar electrocatalytic activity for sulfur ion reduction based on equation (3) [62,63]:

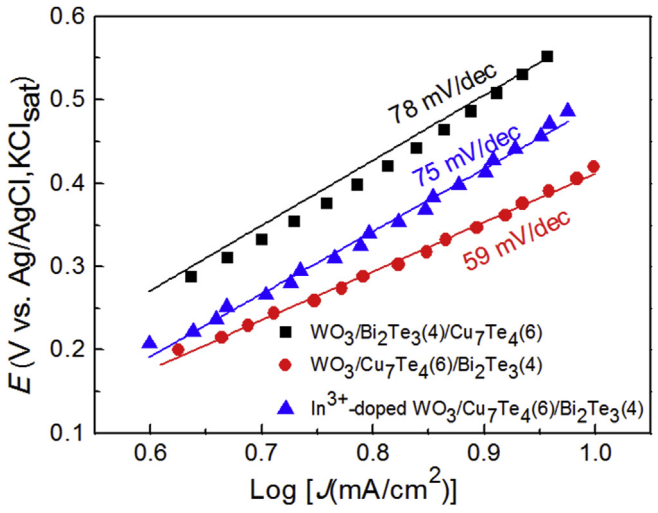

Fig. 10. Linear regions of Tafel plots of co-binary material coated on the WO_3 electrode.

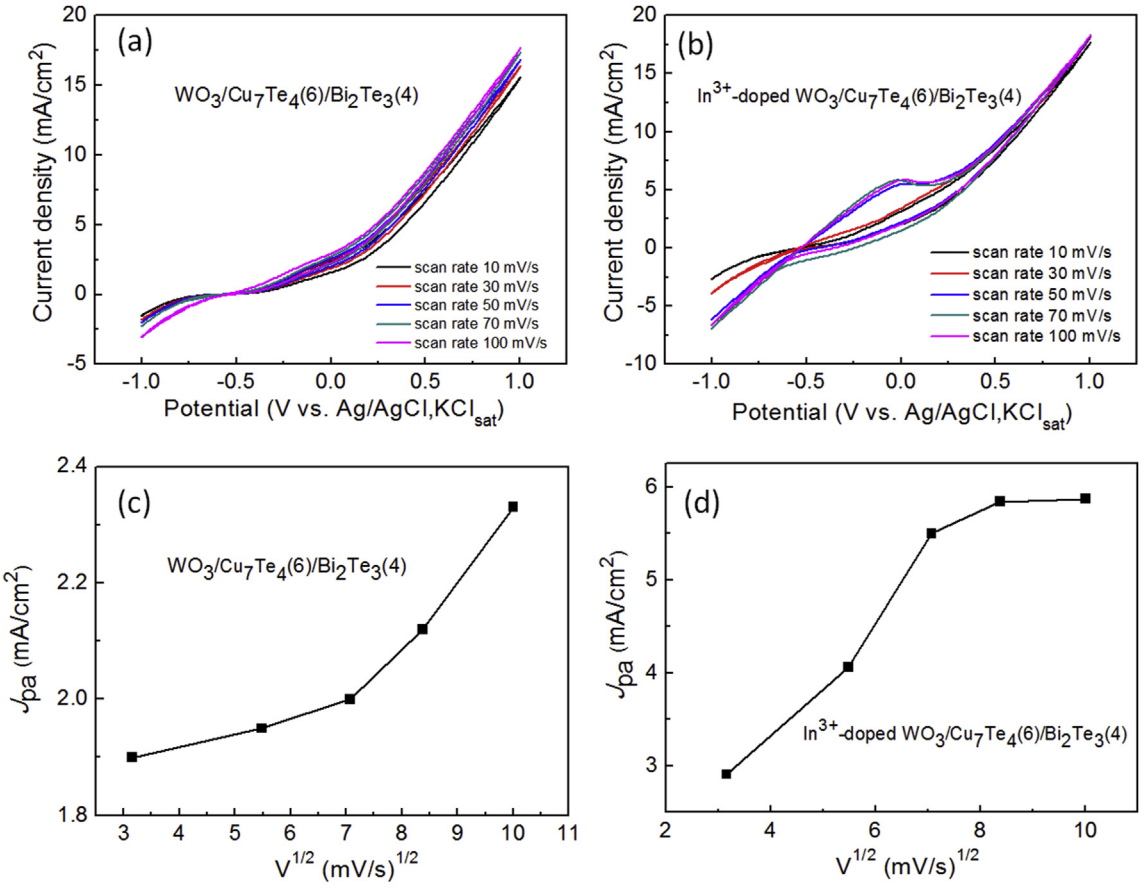

Fig. 11. (a, b) Cyclic voltammetry measurements at various scan rates and (c, d) plots of anodic peak current density values (J_{pa}) vs. the square root of the potential scan rate ($V^{1/2}$) for undoped and In^{3+}-doped $WO_3/Cu_7Te_4(6)/Bi_2Te_3(4)$ electrodes, respectively.

$$S_x^{2-} + 2xe^- \rightarrow S_{x-1}^{2-} + xS^{2-} \quad (3)$$

The electrochemical reaction for the S^{2-} insertion/extraction process at the Cu_7Te_4 and Bi_2Te_3 surfaces can be expressed by equations (4) and (5), respectively [64,65]:

$$Cu_7Te_3 + xS^{2-} \leftrightarrow Cu_7Te_3S_x + 2xe^-, \quad (4)$$

$$Bi_2Te_3 + xS^{2-} \leftrightarrow Bi_2Te_3S_x + 2xe^-. \quad (5)$$

When the scan rate was increased, the CV curves for both electrodes became more symmetrical, with more positive anodic and negative cathodic current densities. This corresponds to the incorporation of higher densities of protons and electrons into the electrode by polarization in the electrode [66,67]. In addition, after In^{3+} doping in WO_3, the positive and negative current densities in the anodic and cathodic curves were higher, which indicated that electron transfer became easier after In^{3+} doping (Fig. 11(b)). This could be attributed to the improved electrochemical stability with a larger ion storage capacity in the electrode [67]. For the scan rates from 50 to 100 mV/s, the peaks at near-zero voltage in the anodic region were attributed to the irreversible reduction of indium and corresponded to faster ion intercalation in the WO_3 film by the reduction process. This is similar to previous reports for vanadium-doped WO_3 and is considered a feature of the typical supercapacitor [68,69]. The anodic peak current density values (J_{pa}) were plotted against the square root of the potential scan rate ($V^{1/2}$) in Fig. 11(c and d) for the undoped and In^{3+}-doped $WO_3/Cu_7Te_4/Bi_2Te_3$ electrodes, respectively. An increase in J_{pa} was observed in both electrodes at increased potential scan rate. This indicated a diffusional limitation of the S_x^{2-}/S^{2-} redox reaction, i.e., the rate-determining step was controlled by the diffusion of sulfur ions in these electrodes [70]. The specific capacity (C_s) can be calculated from the CV curves using equation (6) [71,72]:

$$C_S = \frac{I\Delta U}{3.6 \times mV}, \quad (6)$$

where I is the average current value in the CV curves, ΔU is the operating potential range, m is the weight of active materials ($m = 0.0066 \pm 0.0001$ g for the undoped and In^{3+}-doped electrodes), and V is the potential scan rate. The values of C_s are plotted in Fig. 12(a). The highest C_s value of 90.2 mA h/g was obtained for the In^{3+}-doped sample at a scan rate of 10 mV/s, and it decreased to 9.4 mA h/g as the scan rate was increased to 100 mV/s. Thus, C_s is inversely proportional to the scan rate, owing to the slower rate of ion diffusion into the electrodes that reduces the capacity at the high scan rates [73,74]. On the other hand, a lower scan rate leads to a larger capacity through a higher diffusion rate [75]. It is also noted that the In3+-doped electrode had higher C_s value than the undoped one, which is mainly due to two possible reasons: (1) the inclusion of multivalent metal cations (i.e., In^{3+}, W^{6+}, Cu^{2+}, and Bi^{3+}), and (2) the presence of a strong electro-activation effect from the inclusion of In^{3+} in WO_3. Similar to ZnO, WO_3 is electrocatalytically inactive with respect to proton reduction kinetics, and its CV loop does not display a large integrated area [72]. Thus, the In^{3+} doping in WO_3 improved its capacity by increasing the surface-

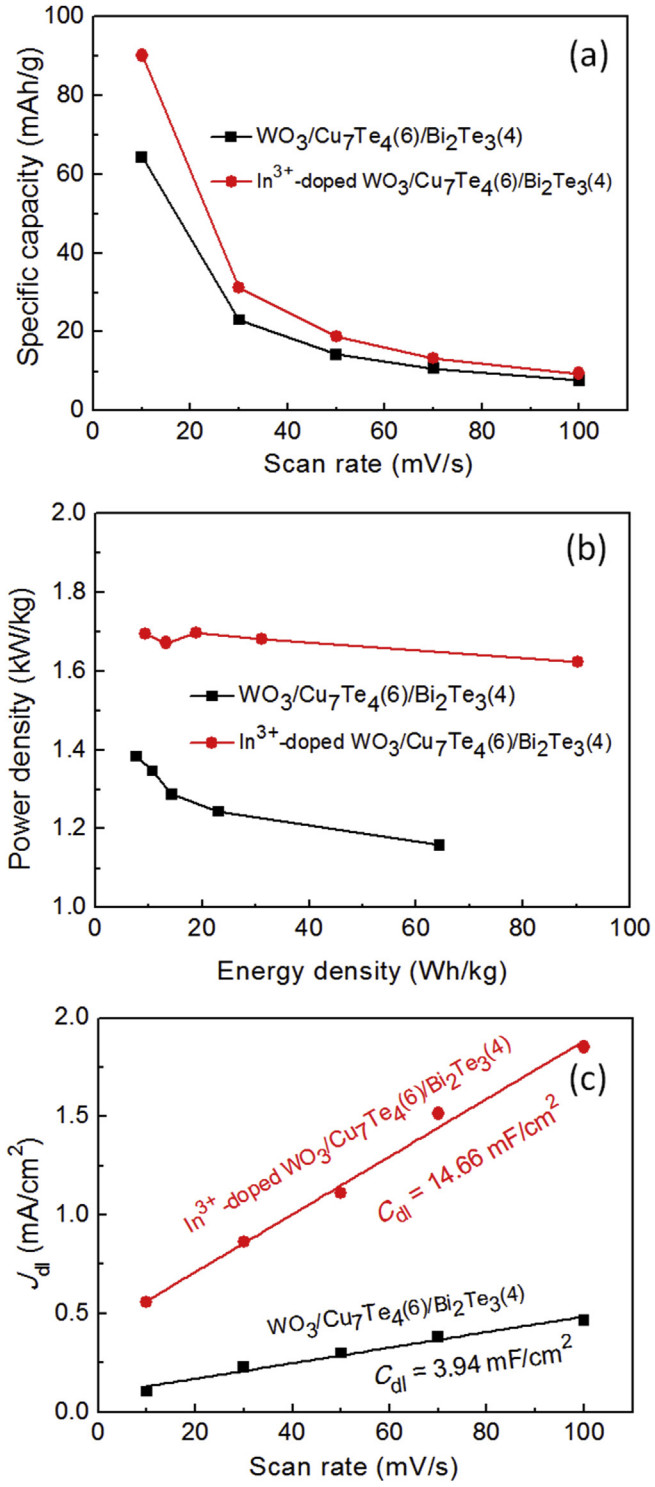

Fig. 12. (a) Specific capacitance, (b) Ragone plot, and (c) determination of the double-layer capacitances for undoped and In^{3+}-doped $WO_3/Cu_7Te_4(6)/Bi_2Te_3(4)$ electrodes.

to-volume ratio, as more atoms are located on the surface of the heterostructure to interact with sulfur ions from the electrolyte, resulting in faster charge transfer and better conductivity. This could mean enhanced capacitor characteristics for the electrode [75]. To confirm the potential of our synthesized material (In^{3+}-doped $WO_3/Cu_7Te_4/Bi_2Te_3$) for electrochemical and energy storage applications, its specific capacity is compared to various reported materials in Table 1, together with the electrolytes used and the scan rate/current density regimes. Our material has relatively higher specific capacity than all but two in the Table 1, affirming its feasibility while indicating room for improvement before practical use in energy storage devices and rechargeable batteries in the future.

The specific energy density (ED) and power density (PD) of the electrodes were determined from the specific capacity values using equations (7) and (8), respectively [83]:

$$ED = \frac{C_S(\Delta V)^2}{2}, \tag{7}$$

$$PD = \frac{C_S(\Delta V)s}{2}, \tag{8}$$

where ΔV is the potential window ($\Delta V = 2$ V). The variable s in equation (8) is the potential scan rate. Fig. 12(b) illustrates the Ragone plot (PD vs. ED) for the undoped and In^{3+}-doped $WO_3/Cu_7Te_4(6)/Bi_2Te_3(4)$ heterostructures. After In^{3+} doping, PD reached 1.7 kW/kg at the highest ED equal to 18.85 Wh/kg. These values are superior to those of the undoped electrode (1.38 kW/kg at 7.69 Wh/kg), which further demonstrated that the In^{3+} doping may improve the electrochemical performance of electrodes.

To further reveal the influence of In^{3+} doping on the electrochemical active surface area of WO_3, Cu_7Te_4, and Bi_2Te_3, the double-layer capacitance (C_{dl}) was measured for the as-synthesized electrodes. C_{dl} was measured using the cyclic voltammogram at different scan rates recorded in the non-Faradic region of the potential window (−0.5 to 0.1 V vs. Ag/AgCl). In this potential region, the average currents during the forward and reverse scan were calculated, and half of their difference was taken as the charging of the double layer instead of any redox reactions [84]. A plot was made based on the equation $J_{dl} = s \times C_{dl}$, in which C_{dl} is determined using the time derivative of the capacitance with the linear slope of the plot between $J_{dl} = J_{anodic} - J_{cathodic}$ and the potential scan rate (s) [85,86]. As shown in Fig. 12(c), the current is linearly dependent on the potential scan rate, demonstrating that the films acted as a simple capacitor in this potential region [84]. The calculated C_{dl} value of the electrode with In^{3+}-doped WO_3 (15 mF/cm^2) was higher than that of the undoped electrode (4 mF/cm^2), indicating increased active surface area, charge transfer capability, and conductivity. These changes could result in enhanced electrochemical HER as well as catalytic performance and stability [85].

3.6. Chronoamperometry

In our CA experiment, the potential of the working electrode was stepped from its rest potential of 0 V to −1.0 V vs. Ag/AgCl for 10 s, and then with a reversed potential of 0 V to +1.0 V vs. Ag/AgCl for the next 10 s. A current from Faradic processes is induced at the electrode by the potential step as a function of time, as illustrated in Fig. 13(a and b) for the undoped and In^{3+}-doped electrodes, respectively. An asymmetrical behavior was observed for both electrodes, with the anodic current being smaller than the cathodic current, suggesting fast kinetics of ion deintercalation and intercalation in the electrode surfaces, respectively [87]. The response time for the colored (t_c) and bleached (t_b) states is the respective time required for the anodic (charging, deintercalation) and cathodic (discharging, intercalation) currents to achieve a steady-state level after the application of reactive voltages. During the coloration process, the electrode transitions from an insulator to a conductor. Consequently, in the current study, the coloration kinetics was slower than the bleaching kinetics due to the higher current through the conductor electrode. Meanwhile, a rapid decay

Table 1
Comparison of electrodes, electrolyte compositions, and specific capacities for energy storage devices.

Electrode	Electrolyte	Specific capacity (mAh/g)	Scan rate or current density regime	Ref.
Cu_2S–Ag_2S composite	KOH	150.1	10 mV/s	[4]
Sphere-like MoS_2	Na_2SO_4	20.6	5 mV/s	[76]
Bi_2S_3 thin film	Na_2SO_4	56.2	5 mV/s	[77]
Sm_2Te_3 thin films	$LiClO_4$–PC	52.0	5 mV/s	[78]
Flower-like $Cu_{1.8}S$ nanostructures	KOH	224.5	5 mV/s	[79]
$MoTe_2$/polyaniline	H_2SO_4	76.2	0.4 A/g	[80]
$NiFe_2O_4/MoS_2$ composite	KOH	84.3	1 A/g	[81]
MnS_2/MoS_2 thin films	Na_2SO_4	57.0	5 mV/s	[82]
WO_3/In^{3+}-doped [$Cu_{2-x}Te/Bi_2Te_3$]	Polysulfide	17.0	10 mV/s	[25]
In^{3+}-doped WO_3/[Cu_7Te_4/Bi_2Te_3]	Polysulfide	90.2	10 mV/s	This work

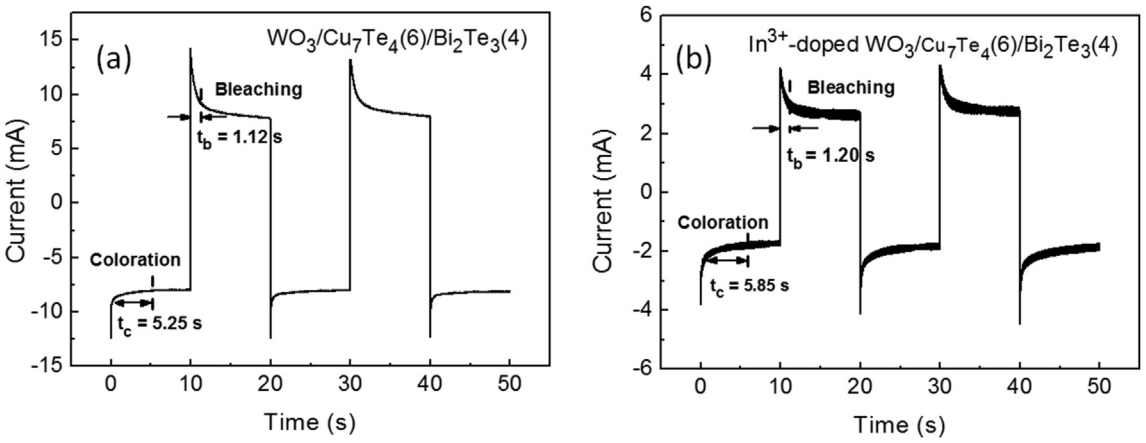

Fig. 13. Chronoamperometry of (a) undoped and (b) In^{3+}-doped WO_3 electrodes coated by $Cu_7Te_4(6)/Bi_2Te_3(4)$.

in the current was observed in the bleaching process due to the conductor-to-insulator transition [88], and the ionic dispersion dynamics was affected by the different surface characteristics during the oxidation and reduction processes [89]. For the In^{3+}-doped $WO_3/Cu_7Te_4/Bi_2Te_3$ electrode, the response times of the bleached and colored states were 1.20 and 5.85 s, respectively, which were shorter than those for the undoped electrode ($t_b = 1.12$ s and $t_c = 5.25$ s). A possible explanation is that the doping of In^{3+} ions into the WO_3 lattice created some vacant sites in the host lattice that caused more oxygen to adsorb on the WO_3 surface, thereby creating more active sites for improved electrode response. Thus, the In^{3+}-doped electrode had a faster response time, due to the easy insertion and deinsertion of S^{2-} and Na^+ ions into the large active sites on the interface of the negative and positive electrodes, respectively [90]. Furthermore, the doped electrode had more electron transport channels (i.e., a higher electrical conductivity) in its three-dimensional heterostructure [91].

3.7. Chronocoulometry

CC is an electrochemical measurement process, which was used to investigate the effective surface area of the undoped and In^{3+}-doped $WO_3/Cu_7Te_4/Bi_2Te_3$ electrodes by applying the potential of +1.0 V vs. Ag/AgCl in a polysulfide electrolyte solution. Fig. 14(a) presents the plots of the *Q-t* characteristics for the undoped and In^{3+}-doped electrodes. A recording charge (*Q*) with increasing time response was corresponded the ion concentration gradients in the solution adjacent to the electrode surface [92]. The absorption of electro-active species, the rate constant, and the mechanisms for the chemical reactions of protons/electrons can be investigated through the Anson equation [93]:

$$Q = \frac{2nFACD^{1/2}t^{1/2}}{\pi^{1/2}}, \tag{9}$$

where *Q* is the charge obtained from integrating the current over time, *n* is the number of electrons transferred ($n = 1$), *F* is Faraday's constant (96,485.3C/mol), *A* is the area of the electrode ($A = 1$ cm^2), *C* is the concentration of sulfur atoms in the polysulfide electrolyte and CuS counter electrode (0.00325 mol/cm^3) penetrating the working electrode, and *D* is the diffusion coefficient. The charge passed in reducing the diffusion reaction is dependent on the square root of time ($t^{1/2}$). The effective surface area can be described by the calculated redox diffusion coefficient and determined from the linear regression slopes of the Anson plot (Q-$t^{1/2}$), as shown in Fig. 14(b and c) for the undoped and In^{3+}-doped electrodes, respectively. The redox diffusion coefficient (*D*) was calculated from the linear regression slopes of the Anson plot, and its value increased from 7.59 × 10^{-12} cm^2/s for the undoped electrode to 13.73 × 10^{-12} cm^2/s after In^{3+} doping in WO_3 for the heterostructure electrode. These results are consistent with the slightly lower J_{pa} in the CV performance from Fig. 9(d). The higher diffusion coefficient in the In^{3+}-doped electrode led to the larger coloration transition. This result is reasonable given that the doping enhanced the ion storage capacity to allow the insertion/extraction of more ions into/from the host material. Thus, a larger ion diffusion coefficient indicates faster movement of S^{2-} and Na^+ ions to the working electrode and counter electrode, respectively, leading to a shorter switching time of the charging and discharging states and shortened effective diffusion path.

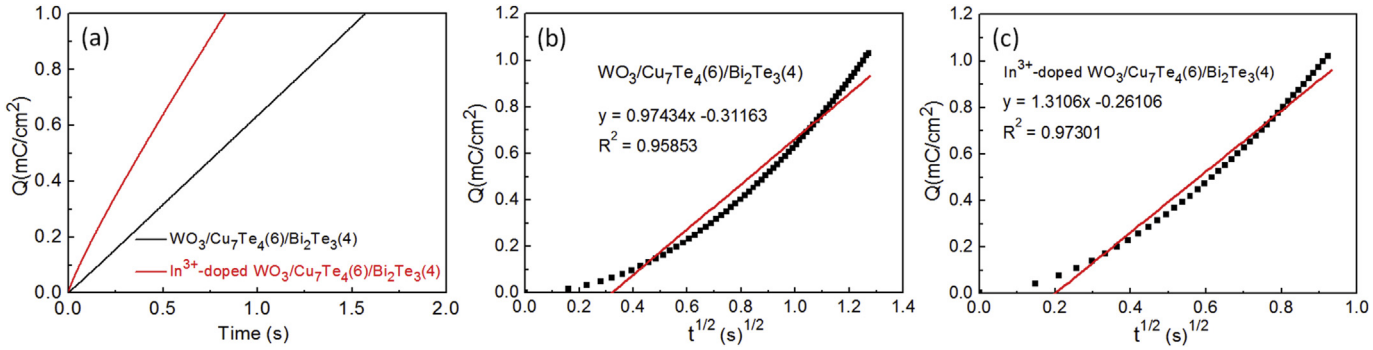

Fig. 14. (a) Chronocoulometry and (b, c) Anson plot (Q-$t^{1/2}$) of undoped and In^{3+}-doped $WO_3/Cu_7Te_4(6)/Bi_2Te_3(4)$ electrodes, respectively.

3.8. Linear sweep voltammetry

The electrolytic production of the undoped and In^{3+}-doped $WO_3/Cu_7Te_4/Bi_2Te_3$ electrodes was investigated using their electrocatalytic activity. The LSV curves of the two electrodes are displayed in Fig. 15 with a voltage range of 0–1.0 V vs. Ag/AgCl and a scan rate of 100 mV/s at 298 K. The results showed the intrinsic catalytic activity corresponding to the substantially different current density over the potential. Therefore, the electrochemically active surface area plays an important role in determining the discharge process of the electrode [94]. The In^{3+}-doped $WO_3/Cu_7Te_4/Bi_2Te_3$ electrode has a higher oxidative current response than the undoped electrode during the LSV scan. This indicates that the former electrode had more energetic electrons and faster electro-kinetics, which can also be attributed to hydrogen generation in the water decomposition reaction [95]:

$$2H_2O + 2e^- \rightarrow H_2 + 2OH^-. \quad (10)$$

In addition, the threshold potentials are indicated by the intercept on the x-axis, referred to as the breakdown voltage. The In^{3+}-doped $WO_3/Cu_7Te_4/Bi_2Te_3$ electrode had a much lower breakdown voltage of 0.27 V compared with 0.46 V for the undoped electrode. A lower breakdown voltage can allow the use of smaller, cheaper, and safer power supply by reducing the voltage required to initiate breakdown for the generating electrons or ions into the discharge region [96].

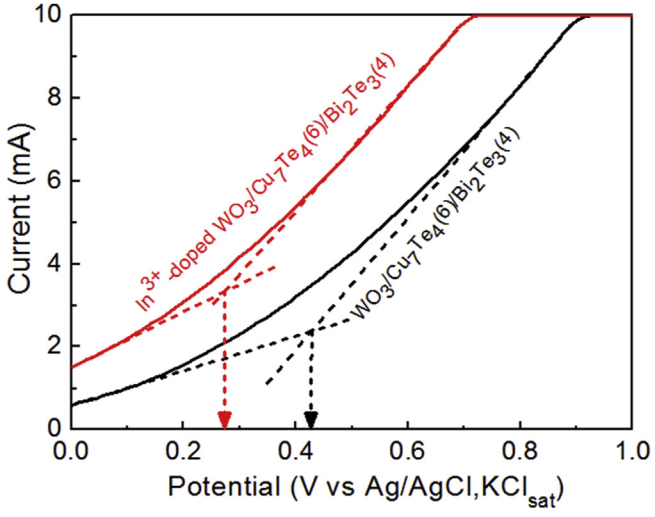

Fig. 15. Linear sweep voltammetry of undoped and In^{3+}-doped $WO_3/Cu_7Te_4(6)/Bi_2Te_3(4)$ electrodes.

4. Conclusions

Undoped and In^{3+}-doped WO_3 films were coated with rhombohedral Bi_2Te_3 thin films and

hexagonal Cu_7Te_4 NCs for use in energy storage applications. We systematically studied the influence of In^{3+} doping on the behavior of the WO_3 electrode as an electron acceptor. The CV curves of the undoped and In^{3+}-doped WO_3 electrodes after coating with Bi_2Te_3 thin film and Cu_7Te_4 NCs showed Faradic pseudocapacitance behavior. The doped In^{3+} cation diffused inside the WO_3 lattice and was involved in the insertion-removal exchange process of electrons, with additional electrochemical S^{2-} insertion/extraction occurring at the Cu_7Te_4/Bi_2Te_3 and polysulfide electrolyte surfaces. In addition, increases in the active surface area, charge transfer capability, and conductivity of the electrode after In^{3+} doping may enhance the electrochemical HER, catalytic performance, and stability of related devices. Our overall results showed that Cu_7Te_4 and Bi_2Te_3 on undoped and In^{3+}-doped WO_3 may be used to fabricate energy storage devices or future electrochemical energy storage applications for hydrogen (oxygen) evolution reactions. However, changing the doping element or using other metal chalcogenide thin films may further improve the specific capacitance and reduce the charge transfer resistance in these materials. Alternatively, these nanocomposite thin films can be synthesized with graphene oxide (GO) to improve the electrochemical property, by utilizing the highly conductive GO and the specific capacity of the electrochemically active pseudocapacitors. These findings can lead to substantial enhancements in the energy and power densities of electrochemical and energy storage devices.

Declaration of competing interest

There are no conflicts of interest to declare.

CRediT authorship contribution statement

Supitchaya Buathet: Conceptualization, Methodology. **Kodchakorn Simalaotao:** Data curation, Writing - original draft, Validation, Writing - review & editing. **Pakpoom Reunchan:** Data curation, Writing - original draft, Validation, Writing - review & editing. **Veeramol Vailikhit:** Validation, Writing - review & editing. **Pichanan Teesetsopon:** Validation, Writing - review & editing. **Duanghatai Raknual:** Visualization, Investigation. **Nareerat Kitisripanya:** Validation. **Auttasit Tubtimtae:** Supervision, Writing - original draft.

Acknowledgment

The authors gratefully acknowledge the Kasetsart University

Research and Development Institute, Bangkok, Thailand (Grant No. 108.61). Finally, we thank Ms. Panitee Suttiyarak for her contribution to this research.

Appendix A. Supplementary data

Supplementary data to this article can be found online at https://doi.org/10.1016/j.electacta.2020.136049.

References

[1] L.N. Qiao, H.C. Wang, Y. Shen, Yuan-Hua Lin, Ce-Wen Nan, Visible-active photocatalytic behaviors observed in nanostructured lead chalcogenides PbX (X = S, Se, Te), AIP Adv. 6 (2016), 015108.

[2] D.J. Lewis, P. Kevin, O. Bakr, C.A. Muryn, M.A. Malika, P. O'Brien, Routes to tin chalcogenide materials as thin films or nanoparticles: a potentially important class of semiconductor for sustainable solar energy conversion, Inorg. Chem. Front. 1 (2014) 577–598.

[3] H. Luo, B. Wang, Y. Li, T. Liu, W. You, D. Wang, Core-shell structured Fe_3O_4@NiS nanocomposite as high-performance anode material for alkaline nickel-iron rechargeable batteries, Electrochim. Acta 231 (2017) 479–486.

[4] S.A. Pawar, D.S. Patil, J.C. Shin, Electrochemical battery-type supercapacitor based on chemosynthesized Cu_2S–Ag_2S composite electrode, Electrochim. Acta 259 (2018) 664–675.

[5] N. Nair, B.R. Sankapal, Nested CdS@HgS core–shell nanowires as supercapacitive Faradaic electrode through simple solution chemistry, Nano-Structures & Nano-Objects 10 (2017) 159–166.

[6] J. Li, J. Lin, Facile fabrication of FeP/CdS for H_2 evolution, Mater. Lett. 221 (2018) 289–292.

[7] X.L. Yin, L.L. Li, D.C. Li, Z.J. Li, Y.X. Wang, X.J. Kong, J.S. Zhao, J.H. Jiang, J.C. Qian, D.H. Pang, X.X. Du, J.M. Dou, Noble-metal-free CdS@MoS_2 core-shell nanoheterostructures for efficient and stabilized visible-light-driven H_2 generation, Int. J. Hydrogen Energy 44 (2019) 16657–16666.

[8] D. Teweldebrhan, V. Goyal, A.A. Balandin, Exfoliation and characterization of bismuth telluride atomic quintuples and quasi-two-dimensional crystals, Nano Lett. 10 (2010) 1209–1218.

[9] F. Tu, J. Xie, G. Cao, X. Zhao, Self-assembly of Bi_2Te_3-nanoplate/graphene-nanosheet hybrid by one-pot route and its improved Li-storage properties, Materials 5 (2012) 1275–1284.

[10] C. Chiritescu, C. Mortensen, D.G. Cahill, D. Johnson, P. Zschack, Lower limit to the lattice thermal conductivity of nanostructured Bi_2Te_3-based materials, J. Appl. Phys. 106 (2009), 073503.

[11] S. Khan, M. Chouhan, Review of bismuth telluride (Bi_2Te_3) nanostructure, characterization and properties, International Journal of Emerging Technology in Computer Science & Electronics 21 (2016) 235–238.

[12] H.J. Goldsmid, Bismuth telluride and its alloys as materials for thermoelectric generation, Materials 7 (2014) 2577–2592.

[13] K. Kurosaki, A. Kosuga, H. Muta, S. Yamanaka, Thermoelectric and thermophysical characteristics of Cu_2Te-Tl_2Te pseudo binary system, Mater. Trans. 47 (2006) 1432–1435.

[14] C.C. Lin, W.F. Lee, M.Y. Lu, S.Y. Chen, M.H. Hung, T.C. Chan, H.W. Tsai, Y.L. Chueh, L.J. Chen, Low temperature synthesis of copper telluride nanostructures: phase formation, growth, and electrical transport properties, J. Mater. Chem. 22 (2012) 7098–7103.

[15] X. Wu, J. Zhou, A. Duda, Y. Yan, G. Teeter, S. Asher, W.K. Metzger, S. Demtsu, S.H. Wei, R. Noufi, Phase control of Cu_xTe film and its effects on CdS/CdTe solar cell, Thin Solid Films 515 (2007) 5798–5803.

[16] J.L.F.D. Silva, S.H. Wei, J. Zhou, X. Wu, Stability and electronic structures of Cu_xTe, Appl. Phys. Lett. 91 (2007), 091902.

[17] B.S. Farag, S.A. Khodier, Direct and indirect transitions in copper telluride thin films, Thin Solid Films 201 (1991) 231–240.

[18] A.S. Pashinkin, L.M. Pavlova, Standard functions of formation and thermodynamic stability of compounds in the Cu-Te system, Inorg. Mater. Engl. Transl. 41 (2005) 1050–1054.

[19] G.B. Palmer, K.R. Poeppelmeier, T.O. Mason, $Zn_{2-x}Sn_{1-x}In_{2x}O_{4-\delta}$: an indium-substituted spinel with transparent conducting properties, J. Solid State Chem. 134 (1997) 192–197.

[20] M. Kazazi, P. Abdollahi, M. Mirzaei-Moghadam, High surface area TiO_2 nanospheres as a high-rate anode material for aqueous aluminium-ion batteries, Solid State Ionics 300 (2017) 32–37.

[21] M. Tahir, N.A.S. Amin, Indium-doped TiO_2 nanoparticles for photocatalytic CO_2 reduction with H_2O vapors to CH_4, Appl. Catal. B Environ. 162 (2015) 98–109.

[22] P. Srathongluan, R. Kuhamaneechot, P. Sukthao, V. Vailikhit, S. Choopun, A. Tubtimtae, Photovoltaic performances of $Cu_{2-x}Te$ sensitizer based on undoped and indium^{3+}-doped TiO_2 photoelectrodes and assembled counter electrodes, J. Colloid Interface Sci. 463 (2016) 222–228.

[23] T. Maiyalagan, B. Viswanathan, Catalytic activity of platinum/tungsten oxide nanorod electrodes towards electro-oxidation of methanol, J. Power Sources 175 (2008) 789–793.

[24] Y. Liu, C. Luo, H. Liu, Tungsten trioxide promoted selective conversion of cellulose into propylene glycol and ethylene glycol on a ruthenium catalyst, Angew. Chem., Int. Ed. Engl. 51 (2012) 3249–3253.

[25] R. Sreerung, D. Raknual, V. Vailikhit, P. Teesetsopon, N. Kitisripanya, A. Tubtimtae, Structural and electrochemical studies of undoped and In^{3+}-doped cobinary $Cu_{2-x}Te$ and Bi_2Te_3 thin films for aqueous Na–S batteries, Ceram. Int. 45 (2019) 17305–17317.

[26] J. Heyd, G. Scuseria, M. Ernzerhof, Hybrid functionals based on a screened Coulomb potential, J. Chem. Phys. 118 (2003) 8207–8215.

[27] G. Kresse, J. Furthmüller, Efficient iterative schemes for *ab initio* total-energy calculations using a plane-wave basis set, Phys. Rev. B 54 (1996) 11169–11186.

[28] C. Freysoldt, B. Grabowski, T. Hickel, J. Neugebauer, G. Kresse, A. Janotti, C.G. Van de Walle, First-principles calculations for point defects in solids, Rev. Mod. Phys. 86 (2014) 253–305.

[29] M. Binnewies, E. Milke, Thermochemical Data of Elements and Compounds, Wiley-VCH, Weinheim; New York, 1999.

[30] P. Reunchan, S. Ouyang, N. Umezawa, H. Xu, Y. Zhang, J. Ye, Theoretical design of highly active $SrTiO_3$-based photocatalysts by a codoping scheme towards solar energy utilization for hydrogen production, J. Mater. Chem. 1 (2013) 4221–4227.

[31] N. Buatong, I.M. Tang, W. Pon-On, The study of metal sulfide as efficient counter electrodes on the performances of CdS/CdSe/ZnS-co-sensitized hierarchical TiO_2 sphere quantum dot solar cells, Nanoscale Res. Lett. 12 (1–9) (2017) 170.

[32] S.S. Shendage, V.L. Patil, S.A. Vanalakar, S.P. Patil, N.S. Harale, J.L. Bhosale, J.H. Kim, P.S. Patil, Sensitive and selective NO_2 gas sensor based on WO_3 nanoplates, Sensor. Actuator. B Chem. 240 (2017) 426–433.

[33] Y. Liang, W. Wang, B. Zeng, G. Zhang, J. Huang, J. Li, T. Li, Y. Song, X. Zhang, Raman scattering investigation of Bi_2Te_3 hexagonal nanoplates prepared by a solvothermal process in the absence of NaOH, J. Alloy, Compd 509 (2011) 5147–5151.

[34] D.C. Pereira, D.L.A. de Faria, V.R.L. Constantino, CuII Hydroxy Salts: characterization of layered compounds by vibrational spectroscopy, J. Braz. Chem. Soc. 17 (2006) 1651–1657.

[35] M.H. Manghnani, A. Hushur, T. Sekine, J. Wu, J.F. Stebbins, Q. Williams, Raman, Brillouin, and nuclear magnetic resonance spectroscopic studies on shocked borosilicate glass, J. Appl. Phys. 109 (2011), 113509.

[36] R. Hussin, N.S. Leong, N.S. Alias, Structural investigation of crystalline host phosphor cadmium tellurite systems, J. Fund. Sci. 5 (2009) 17–27.

[37] S. Bai, K. Zhang, L. Wang, J. Sun, R. Luo, D. Li, A. Chen, Synthesis mechanism and gas-sensing application of nanosheet-assembled tungsten oxide microspheres, J. Mater. Chem. 2 (2014) 7927–7934.

[38] N.S. Tagiara, D. Palles, E.D. Simandiras, V. Psycharis, A. Kyritsis, E.I. Kamitsos, Synthesis, thermal and structural properties of pure TeO_2 glass and zinc-tellurite glasses, J. Non-Cryst. Solids 457 (2017) 116–125.

[39] Q. Yang, Q. Qian, D.D. Chen, Q.Y. Zhang, Z.H. Jiang, Enhanced thermal stability and broadened Raman scattering of tellurite glasses by co-doping heavy metal oxides, J. Optoelectron. Adv. Mater. 3 (2009) 565–568.

[40] J. Bielecki, S.F. Parker, D. Ekanayake, S.M.H. Rahman, L. Börjesson, M. Karlsson, Short-range structure of the brownmillerite-type oxide $Ba_2In_2O_5$ and its hydrated proton-conducting form $BaInO_3H$, J. Mater. Chem. 2 (2014) 16915–16924.

[41] R. Cárdenas, J. Torres, J.E. Alfonso, Optical characterization of MoO_3 thin films produced by continuous wave CO_2 laser-assisted evaporation, Thin Solid Films 478 (2005) 146–151.

[42] J. Clatot, G. Campet, A. Zeinert, C. Labrugère, M. Nistor, A. Rougier, Low temperature Si doped ZnO thin films for transparent conducting oxides, Sol. Energy Mater. Sol. Cells 95 (2011) 2357–2362.

[43] L.M. Bertus, C. Faure, A. Danine, C. Labrugere, G. Campet, A. Rougier, A. Duta, Synthesis and characterization of WO_3 thin films by surfactant assisted spray pyrolysis for electrochromic applications, Mater. Chem. Phys. 140 (2013) 49–59.

[44] Z. Zhuang, Q. Peng, J. Liu, X. Wang, Y. Li, Indium hydroxides, oxyhydroxides, and oxides nanocrystals series, Inorg. Chem. 46 (2007) 5179–5187.

[45] F.A. Akgul, G. Akgul, N. Yildirim, H.E. Unalan, R. Turan, Influence of thermal annealing on microstructural, morphological, optical properties and surface electronic structure of copper oxide thin films, Mater. Chem. Phys. 147 (2014) 987–995.

[46] M.C. Biesinger, L.W.M. Lau, A.R. Gerson, R.S. Smart, Resolving surface chemical states in XPS analysis of first row transition metals, oxides and hydroxides: Sc, Ti, V, Cu and Zn, Appl. Surf. Sci. 257 (2010) 887–898.

[47] B. Zeynizadeh, Z. Shokri, I. Mohammadzadeh, The immobilized copper species on nickel ferrite ($NiFe_2O_4$@Cu): a magnetically reusable nanocatalyst for one-pot and quick reductive acetylation of nitroarenes to N-arylacetamides, J. Iran. Chem. Soc. (2019), https://doi.org/10.1007/s13738-019-01818-9.

[48] J.K. Reddy, B. Srinivas, V. Durga Kumari, M. Subrahmanyam, Sm^{3+}-Doped Bi_2O_3 photocatalyst prepared by hydrothermal synthesis, chem. Cat, Inside Chem. 1 (2009) 492–496.

[49] Č. Jovalekić, M. Pavlović, X-ray photoelectron spectroscopy study of $Bi_4Ti_3O_{12}$ ferroelectric ceramics, Appl. Phys. Lett. 72 (1998) 1051.

[50] H. Kong, J.B. Yeo, H.Y. Lee, A study on the properties of tellurium-oxide thin films based on the variable sputtering gas ratio, J. Kor. Phys. Soc. 66 (2015) 1744–1749.

[51] C. Liu, Z.G. Neale, G. Cao, Understanding electrochemical potentials of cathode materials in rechargeable batteries, Mater, Today Off. 19 (2016) 109–123.

[52] H.C. Chen, D.J. Jan, C.H. Chen, K.T. Huang, Bond and electrochromic properties

of WO_3 films deposited with horizontal DC, pulsed DC, and RF sputtering, Electrochim. Acta 93 (2013) 307–313.
[53] D.S. Dalavi, R.S. Devan, R.A. Patil, R.S. Patil, Y.R. Ma, S.B. Sadale, I.Y. Kim, J.H. Kim, P.S. Patil, Efficient electrochromic performance of nano-particulate WO_3 thin films, J. Mater. Chem. C 1 (2013) 3722–3728.
[54] J. Zhang, Y. Zhu, C. Chen, X. Yang, C. Li, Carbon nanotubes coated with platinum nanoparticles as anode of biofuel cell, Particuology 10 (2012) 450–455.
[55] J.D. Bocarsly, D. Hirai, M.N. Ali, R.J. Cava, Superconducting phase diagram of In_xWO_3 synthesized by indium deintercalation, EPL (Europhysics Letters) 103 (2013) 17001.
[56] M. Meenakshi, V. Gowthami, P. Perumal, R. Sivakumar, C. Sanjeeviraja, Influence of dopant concentration on the electrochromic properties of tungsten oxide thin films, Electrochim. Acta 174 (2015) 302–314.
[57] M. Sun, Y. Chen, G. Tian, A. Wu, H. Yan, H. Fu, Stable mesoporous $ZnFe_2O_4$ as an efficient electrocatalyst for hydrogen evolution reaction, Electrochim. Acta 190 (2016) 186–192.
[58] X. Tong, P. Yang, Y. Wang, Y. Qin, X. Guo, Enhanced photoelectrochemical water splitting performance of TiO_2 nanotube arrays coated with an ultrathin nitrogen-doped carbon film by molecular layer deposition, Nanoscale 6 (2014) 6692–6700.
[59] N. Zhang, J. Lei, J. Xie, H. Huang, Y. Yu, MoS_2/Ni_3S_2 nanorod arrays well-aligned on Ni foam: a 3D hierarchical efficient bifunctional catalytic electrode for overall water splitting, RSC Adv. 7 (2017) 46286–46296.
[60] X. Yu, A. Manthiram, Room-temperature Sodium–Sulfur batteries with liquid-phase sodium polysulfide catholytes and binder-free multiwall carbon nanotube fabric electrodes, J. Phys. Chem. C 118 (2014) 22952–22959.
[61] N. Ardoin, J. Winnick, Polysulfide solution chemistry at a CdSe photoanode, J. Electrochem. Soc. 135 (1988) 1719–1722.
[62] Z. Yang, C.Y. Chen, P. Roy, H.T. Chang, Quantum dot sensitized solar cells incorporating nanomaterials, Chem. Commun. (J. Chem. Soc. Sect. D) 47 (2011) 9561–9571.
[63] H.J. Kim, L. Myung-Sik, C.V. Gopi, M. Venkata-Haritha, S.S. Rao, S.K. Kim, Cost-effective and morphology controllable PVP based highly efficient CuS counter electrodes for high-efficiency quantum dot-sensitized solar cells, Dalton Trans. 44 (2015) 11340–11351.
[64] B. Mansour, F. El Akkad, T. Hendeya, Electrical and thermoelectric properties of some copper chalcogenides, Phys. Status Solidi 62 (1980) 495–501.
[65] M. Neupane, S.-Y. Xu, L.A. Wray, A. Petersen, R. Shankar, N. Alidoust, Liu Chang, A. Fedorov, H. Ji, J.M. Allred, Y.S. Hor, T.-R. Chang, H.-T. Jeng, H. Lin, A. Bansil, R.J. Cava, M.Z. Hasan, Topological surface states and Dirac point tuning in ternary topological insulators, Phys. Rev. B 85 (2012), 235406.
[66] X. Qing, S. Liu, K. Huang, K. Lv, Y. Yang, Z. Lu, D. Fang, X. Liang, Facile synthesis of Co_3O_4 nanoflowers grown on Ni foam with superior electrochemical performance, Electrochim. Acta 56 (2011) 4985–4991.
[67] S.S. Kalagi, S.S. Mali, D.S. Dalavi, A.I. Inamdar, H. Im, P.S. Patil, Transmission attenuation and chromic contrast characterization of R.F. sputtered WO_3 thin films for electrochromic device applications, Electrochim. Acta 85 (2012) 501–508.
[68] C.C. Hu, T.W. Tsou, Ideal capacitive behavior of hydrous manganese oxide prepared by anodic deposition, Electrochem. Commun. 4 (2002) 105–109.
[69] M. Toupin, T. Brousse, D. Belanger, Charge storage mechanism of MnO_2 electrode used in aqueous electrochemical capacitor, Chem. Mater. 16 (2004) 3184–3190.
[70] Xiaoxi Liu, Awu Zhou, Yibo Dou, Ting Pan, Mingfei Shao, Jingbin Han, Min Wei, Ultrafast switching of an electrochromic device based on layered double hydroxide/Prussian blue multilayered films, Nanoscale 7 (2015) 17088–17095.
[71] S. Zhang, N. Pan, Supercapacitors performance evaluation, Adv. Energy Mater. 5 (2015) 1401401.
[72] D. Gromadskyi, V. Chervoniuk, S. Kirillov, Cyclic voltammetric study of tin hexacyanoferrate for aqueous battery applications, J. Electrochem. Sci. Eng. 6 (2016) 225–234.
[73] W. Zhou, K. Zhou, X. Liu, R. Hu, H. Liu, S. Chen, Flexible wire-like all-carbon supercapacitors based on porous core–shell carbon fibers, J. Mater. Chem. 2 (2014) 7250–7255.
[74] Y. Wei, H. Liu, Y. Jin, K. Cai, H. Li, Y. Liu, Z. Kang, Q. Zhang, Carbon nanoparticle ionic liquid functionalized activated carbon hybrid electrode for efficiency enhancement in supercapacitors, New J. Chem. 37 (2013) 886–889.
[75] M. Balasubramaniam, S. Balakumar, Exploration of electrochemical properties of zinc antimonate nanoparticles as supercapacitor electrode material, Mater. Sci. Semicond. Process. 56 (2016) 287–294.
[76] K. Krishnamoorty, G. Kumar, Veerasubramani, S. Rhandhakrishnan, S.J. Kim, Supercapacitive properties of hydrothermally synthesized sphere like MoS_2 nanostructures, Mater. Res. Bull. 50 (2014) 499–502.
[77] S.S. Raut, J.A. Dhobale, B.R. Sankapal, SILAR deposited Bi_2S_3 thin film towards electrochemical supercapacitor, Phys. E Low-dimens. Syst. Nanostruct. 87 (2017) 209–212.
[78] V.S. Kumbhar, A.C. Lokhande, N.S. Gaikwad, C.D. Lokhande, Synthesis of samarium telluride thin films by successive ionic layer adsorption and reaction (SILAR) method for supercapacitor application, Mater. Sci. Semicond. Process. 46 (2016) 29–34.
[79] D.R. Kumar, S. Kesavan, M.L. Baynosa, J.J. Shim, Flower-like $Cu_{1.8}S$ nanostructures for high-performance flexible solid-state supercapacitors, Appl. Surf. Sci. 448 (2018) 547–558.
[80] A. Sajedi-Moghaddam, C.C. Mayorga-Martinez, E. Saievar-Iranizad, Z. Sofer, M. Pumera, Exfoliated transition metal dichalcogenide (MX_2; M = Mo, W; X= S, Se, Te) nanosheets and their composites with polyaniline nanofibers for electrochemical capacitors, Appl. Mater. Today 16 (2019) 280–289.
[81] Y. Zhao, L. Xu, J. Yan, W. Yan, C. Wu, J. Lian, Y. Huang, J. Bao, J. Qiu, L. Xu, Y. Xu, H. Xu, H. Li, Facile preparation of $NiFe_2O_4/MoS_2$ composite material with synergistic effect for high performance supercapacitor, J. Alloys Compd. 726 (2017) 608–617.
[82] R.B. Pujari, V.C. Lokhande, U.M. Patil, D.W. Lee, C.D. Lokhande, Controlled sulfurization of $MnCO_3$ microcubes architectured MnS_2 nanoparticles with 1.7 fold capacitance increment for high energy density supercapacitor, Electrochim. Acta 301 (2019) 366–376.
[83] A.K. Samantara, S. Chandra Sahu, A. Ghosh, B.K. Jena, Sandwiched graphene with nitrogen, sulphur co-doped CQDs: an efficient metal-free material for energy storage and conversion applications, J. Mater. Chem. 3 (2015) 16961–16970.
[84] M.J. Gira, K.P. Tkacz, J.R. Hampton, Physical and electrochemical area determination of electrodeposited Ni, Co, and NiCo thin films, Nano Convergence 3 (2016), 6(1-8).
[85] L. Chen, J. Zhang, X. Ren, R. Ge, W. Teng, X. Sun, X. Li, $Ni(OH)_2$-CoS_2 hybrid nanowire array: a superior non-noble-metal catalyst toward the hydrogen evolution reaction in alkaline media, Nanoscale 9 (2017) 16632–16637.
[86] A. Dutta, S. Mutyala, A.K. Samantara, S. Bera, B.K. Jena, N. Pradhan, Synergistic effect of inactive iron oxide core on active nickel phosphide shell for significant enhancement in oxygen evolution reaction activity, ACS Energy Lett (2017) 141–148.
[87] P.M. Kadam, N.L. Tarwal, P.S. Shinde, S.S. Mali, R.S. Patil, A.K. Bhosale, H.P. Deshmukh, P.S. Patil, Enhanced optical modulation due to SPR in gold nanoparticles embedded WO_3 thin films, J. Alloys Compd. 509 (2011) 1729–1733.
[88] S.R. Bathe, P.S. Patil, Electrochromic characteristics of fibrous reticulated WO_3 thin films prepared by pulsed spray pyrolysis technique, Sol. Energy Mater. Sol. Cells 91 (2007) 1097–1101.
[89] S.W. Cai, H.L. Wen, S.Z. Wang, H.J. Niu, C. Wang, X.K. Jiang, X.D. Bai, W. Wang, Electrochromic polymers electrochemically polymerized from 2,5-dithienylpyrrole (DTP) with different triarylamine units: synthesis, characterization and optoelectrochemical properties, Electrochim, Acta 228 (2017) 332–342.
[90] K.S. Usha, R. Sivakumar, C. Sanjeeviraj, Vasant Sathe, V. Ganesan, T.Y. Wang, Improved electrochromic performance of a radio frequency magnetron sputtered NiO thin film with high optical switching speed, RSC Adv. 6 (2016) 79668–79680.
[91] K. Zhang, Y. Wang, X. Ma, H. Zhang, S. Hou, J. Zhao, X. Li, L. Qiang, Y. Li, Three dimensional molybdenum oxide/polyaniline hybrid nanosheet networks with outstanding optical and electrochemical properties, New J. Chem. 41 (2017) 10872–10879.
[92] S.S. Kalagi, D.S. Dalavi, R.C. Pawar, N.L. Tarwal, S.S. Mali, P.S. Patil, Polymer assisted deposition of electrochromic tungsten oxide thin films, J. Alloys Compd. 493 (2010) 335–339.
[93] S. Khazalpour, D. Nematollahi, Electrochemical study of Alamar Blue (resazurin) in aqueous solutions and room-temperature ionic liquid 1-butyl-3-methylimidazolium tetrafluoroborate at a glassy carbon electrode, RSC Adv. 4 (2014) 8431–8438.
[94] Z. Ren, S. Quan, J. Gao, W. Li, Y. Zhu, Y. Liu, B. Chai, Y. Wang, The electrocatalytic activity of IrO_2–Ta_2O_5 anode materials and electrolyzed oxidizing water preparation and sterilization effect, RSC Adv. 5 (2015) 8778–8786.
[95] Y. Xie, Y. Zhao, Electrochemical biosensing based on polypyrrole/titania nanotube hybrid, Mater. Sci. Eng. C 33 (2013) 5028–5035.
[96] J. Sawyer, J. Abboud, Z. Zhang, S. F Adams, Reduction of breakdown threshold by metal nanoparticle seeding in a DC microdischarge, Nanoscale Res. Lett. 10 (2015) 15.